Field Emission at Grain Boundaries: Modeling the Conductivity in Highly Doped Polycrystalline Semiconductors

Nicolas Sommer, Jürgen Hüpkes,* and Uwe Rau

IEK5-Photovoltaik, Forschungszentrum Jülich GmbH, 52425 Jülich, Germany

(Received 20 May 2015; revised manuscript received 23 August 2015; published 22 February 2016)

In this contribution, we elaborate a conductivity model for highly doped polycrystalline semiconductors. The prominent feature of the model is the description of grain-boundary scattering by field emission, i.e., quantum-mechanical tunneling of electrons through potential barriers at grain boundaries. For this purpose, we adapt a theory of Stratton [Theory of field emission from semiconductors, Phys. Rev. 125, 67 (1962)] to double Schottky barriers at grain boundaries. We provide strong evidence that field emission rather than the predominantly applied thermionic emission is the dominant transport path across grain boundaries in semiconductors with carrier concentrations exceeding approximately 10^{19} cm^{-3}. We obtain a comprehensive conductivity model for highly doped polycrystalline semiconductors by combining field emission with two intragrain scattering mechanisms, that are ionized-impurity and electron-phonon scattering. The model is applied to a wide range of literature data in order to show its applicability and explanatory power. The literature data comprise, in particular, transparent conductive oxides with a special emphasis on aluminum-doped ZnO.

DOI: 10.1103/PhysRevApplied.5.024009

I. INTRODUCTION

Transparent conductive oxides (TCOs) are applied in a wide range of applications such as optoelectronic devices due to their unique property of possessing electrical conductivity and transparency in the visible range at the same time [1–6]. Commonly, TCOs such as aluminum-doped ZnO (ZnO : Al), tin-doped indium oxide (In_2O_3 : Sn), and fluorine-doped tin oxide (SnO_2 : F) are degenerately doped to assure high conductivity. Since most TCOs are polycrystalline materials, they are perfect candidates to study the mechanisms that limit the charge-carrier mobility in degenerately doped polycrystalline semiconductors. Understanding these mechanisms is of crucial importance in order to further increase the conductivity in such materials.

A mobility-limiting mechanism is scattering of charge carriers at grain boundaries that so far is predominantly described by thermionic emission [7–10]. However, grain-boundary scattering can comprise two further mechanisms, namely, field emission, also denoted as quantum-mechanical tunneling, and thermionic field emission. Both mechanisms are hardly considered with regard to grain-boundary scattering. Therefore, this work will elaborate a quantitative theory for (thermionic) field emission at grain boundaries based on the work of Stratton [11,12].

The charge-carrier mobility might not be limited by mechanisms located at grain boundaries only, but also by scattering processes within the grain. Thus, we combine grain-boundary scattering with two intragrain scattering mechanisms, namely, ionized-impurity and electron-phonon scattering. In this way, we obtain a comprehensive conductivity model that is applicable to degenerately doped polycrystalline semiconductors.

This work is organized as follows: In Sec. II, we detail the theory of scattering mechanisms in highly doped polycrystalline semiconductors. Most importantly, the description of field emission at grain boundaries is developed, and criteria are given that reveal field emission as the dominant scattering process at grain boundaries. Section III combines the discussed scattering mechanisms in order to obtain a complete conductivity model. The conductivity model is used to fit mobility and conductivity data from the literature that is given as a function of the carrier concentration or measurement temperature. The obtained fit parameters are interpreted with regard to their physical meaning. The proposed conductivity model should be applicable to degenerately doped polycrystalline semiconductors, in general. Nevertheless, in this contribution, we focus on the material class of transparent conductive oxides. Particular emphasis is given to ZnO : Al, which is a prominent TCO representative.

Note finally the extensive Appendixes. There, we critically review the thermionic emission theory, and we develop the analytical description of thermionic field emission at grain boundaries.

II. THEORY OF SCATTERING MECHANISMS

The resistivity of polycrystalline semiconductors may be divided into two contributions: scattering of charge carriers within the grain ρ_g and at grain boundaries ρ_{gb}.

*j.huepkes@fz-juelich.de

Two mechanisms that describe effects within the grain, ionized-impurity and electron-phonon scattering, are discussed in the following. Grain-boundary scattering comprises three possible mechanisms: thermionic emission, field emission, and thermionic field emission.

Further scattering mechanisms within the grain such as dislocation scattering [13–16], neutral impurity scattering [14,16,17], or scattering due to weakly localized electrons [18–20] are not considered in the proposed model. Reasons for the disregard of dislocation and neutral impurity scattering can be found in Refs. [14,16]. Weak localization scattering is beyond the scope of this work. However, it might explain certain features of temperature-dependent Hall effect measurements such as a decreasing resistivity with increasing temperature.

The focus of this section is threefold: (i) The theory of ionized-impurity and electron-phonon scattering is presented. (ii) We elaborate the mathematical description of field emission at grain boundaries. (iii) Two criteria are given that reveal the dominant scattering process at grain boundaries.

A. Ionized-impurity scattering

Highly doped semiconductors such as TCOs with high carrier concentrations n exceeding approximately 10^{19} cm^{-3} possess a large number of ionized donors. They can be intrinsic donors such as oxygen vacancies or extrinsic donors such as aluminum. Ionized donors are charged. Therefore, they scatter charge carriers. The development of the description of ionized-impurity scattering is illustrated in detail by Ellmer [21]. Here, the theory is shortly summarized.

Conwell and Weisskopf assume the ionized impurity to induce a truncated Coulomb potential [22]. However, one has to take into account the screening of the Coulomb potential by free charge carriers reducing the Coulomb potential's strength and scattering ability. Brooks [23] and Herring, and Dingle [24] incorporate the screening into the description of ionized-impurity scattering [25]. The formula for ionized-impurity scattering as derived by Dingle,

$$\mu_{\mathrm{ii}} = \frac{3(\epsilon_r\epsilon_0)^2 h^3}{m^{*2}e^3}\frac{Z_D - Z_A K}{Z_D^2 + Z_A^2 K}\frac{1}{F_{\mathrm{ii}}}, \tag{1}$$

contains the screening function F_{ii}, the static dielectric constant ϵ_r, the vacuum permittivity ϵ_0, and the Planck constant h. Further parameters are the effective mass m^* and the compensation ratio $K = n_A/n_D$ of acceptor n_A and donor n_D concentrations. Z_D and Z_A denote the charge of donors and acceptors, respectively. Note that Eq. (1) assumes only one type of acceptor and donor charge. The analytical expression [26] for the screening function [27],

$$F_{\mathrm{ii}}(\xi_0,\xi_1) = \left\{1 + \frac{4\xi_1}{\xi_0}\left(1 - \frac{\xi_1}{8}\right)\right\}\ln(\xi_0 + 1) - \frac{\xi_0}{\xi_0 + 1} - 2\xi_1\left(1 - \frac{5}{16}\xi_1\right) \tag{2}$$

with

$$\xi_0 = (3\pi^2 n)^{1/3}\frac{\epsilon_r\epsilon_0 h^2}{e^2 m^*} \tag{3}$$

and

$$\xi_1 = 1 - \frac{m_0^*}{m^*}, \tag{4}$$

accounts for the nonparabolicity of the ZnO conduction band by the introduction of an n-dependent effective mass

$$m^*(n) = m_0^*\left\{1 + 2C\frac{\hbar^2}{m_0^*}(3\pi^2 n)^{2/3}\right\}^{1/2}. \tag{5}$$

m_0^* is the effective mass at the minimum of the conduction band, and C is a nonparabolicity parameter.

The description of ionized-impurity scattering by Eq. (1) contains three material parameters that are not well known as they are difficult to measure directly. The mentioned parameters are the donor and acceptor charge $Z_{D,A}$, the compensation ratio K, and the effective mass m^*. A detailed discussion of these material parameters is given in Appendix A.

B. Electron-phonon scattering

The scattering of electrons by phonons in metals is described by the Bloch-Grüneisen law [29–31]. The equation for electron-phonon interaction,

$$\rho_{\mathrm{ph}} = \lambda_{\mathrm{tr}}\frac{4\pi^3 m^* k_B}{he^2}\frac{1}{n}\Theta\left(\frac{T}{\Theta}\right)^5 \times \int_0^{\Theta/T}\frac{x^5 \mathrm{d}x}{[\exp(x) - 1][1 - \exp(-x)]}, \tag{6}$$

contains the electron-phonon coupling constant λ_{tr}, the Debye temperature Θ, the electron charge e, the Boltzmann constant k_B, the Planck constant h, the effective mass m^*, and the carrier concentration n. λ_{tr} and Θ are used as fit parameters to describe temperature-dependent resistivity measurements. Note the reciprocal dependence of ρ_{ph} and n. Assuming constant m^*, λ_{tr}, and Θ, the resistivity due to electron-phonon scattering decreases with increasing carrier concentration. However, the mobility defined by $\mu_{\mathrm{ph}} = (\rho_{\mathrm{ph}} n e)^{-1}$ is independent of the carrier concentration. Figure 1 shows the mobility derived from Eq. (6) as a function of the measurement temperature for various Θ. One observes electron-phonon scattering to be relevant

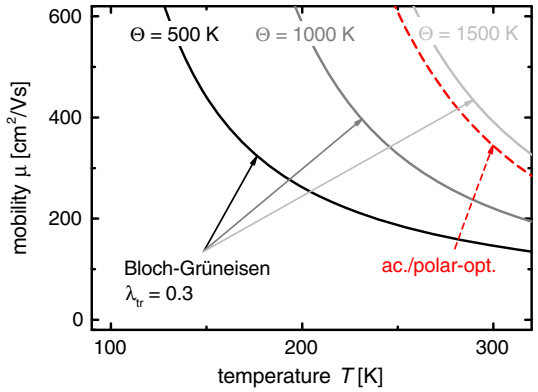

FIG. 1. The mobility is computed as a function of measurement temperature T using either the Bloch-Grüneisen law (solid lines) or the theory of acoustical and polar-optical phonon scattering (dashed line). For the Bloch-Grüneisen law, three different values of the Debye temperature Θ are evaluated: $\Theta = 500$ K (black line), $\Theta = 1000$ K (gray line), and $\Theta = 1500$ K (light gray line). The electron-phonon coupling constant is fixed at $\lambda_{tr} = 0.3$. For acoustical and polar-optical phonon scattering, we apply the theory presented by Look and co-workers [32]. Note that we also use their parameters: $\epsilon_1 = 3.72\epsilon_0$, $T_{po} = 837$ K, $E_1 = 3.8$ eV, $P_{pe} = 0.21$, and $c_l = 1.4 \times 10^{11}$ N m^{-2}. With regard to the effective mass m^*, we refer to Appendix A.

only for temperatures exceeding 150–200 K. Furthermore, Fig. 1 shows lower Θ to imply a stronger electron-phonon scattering and thus a lower mobility.

The Bloch-Grüneisen law has been used to describe electron-phonon scattering in highly doped TCOs before [33–35]. We consider the application of the Bloch-Grüneisen law as a heuristic approach to the description of electron-phonon scattering. Certainly, the Bloch-Grüneisen law takes into account neither the TCO's specific lattice structure nor the covalent and ionic nature of the bonds. Yet, we think that its specific design for degenerate electron systems is a valid argument for its use in highly doped semiconductors. Instead of the Bloch-Grüneisen law, some authors explicitly compute the scattering by optical phonons and by acoustic phonons interacting through deformation or piezoelectric potentials [13,32,36–38]. These models should reproduce the physics of the TCOs more accurately than the Bloch-Grüneisen law. However, they possess free parameters that need to be determined in a rather cumbersome manner for each material, and the models' adjustment to degenerate semiconductors is difficult [38]. To our knowledge, a detailed comparison between both descriptions of electron-phonon scattering has not been performed yet, and it is out of the scope of this work to do so. Certainly, future investigations should comprise the differences and applicability of both theories. Until then, we note that both descriptions of electron-phonon scattering yield a very similar temperature dependence (see Fig. 1).

C. Grain-boundary scattering

Polycrystalline films are composed of small crystalline grains separated by grain boundaries. A grain boundary is a region of disordered atoms between adjacent grains. Disordered atoms imply incomplete atomic bonding resulting in a large number of defects. The defects can trap electrons. The trapping of electrons induces potential barriers at the grain boundaries that may scatter mobile electrons traveling from one grain to another.

The height of the potential barriers at grain boundaries E_B is derived by Seto [7]. Depending on the doping concentration n_D, two different expressions for the barrier height,

$$E_B = \frac{e^2 L^2}{8\epsilon_0\epsilon_r} n_D + E_C, \qquad Ln_D < Q_t, \tag{7a}$$

$$E_B = \frac{e^2 Q_t^2}{8\epsilon_0\epsilon_r} \frac{1}{n_D} + E_C, \qquad Ln_D > Q_t, \tag{7b}$$

may be computed. Here, Q_t denotes the density of occupied traps per area at grain boundaries, ϵ_0 and ϵ_r are the vacuum permittivity and the static dielectric constant, respectively, and L is the lateral grain size. The barrier height as derived by Seto is measured relative to the conduction-band minimum. In the following, we strongly rely on Schottky barrier theory. Since the barrier height in Schottky theory is given with respect to the Fermi level, we modified Seto's barrier height by adding E_C to make it suitable for Schottky theory. In this notation, E_C is measured relative to the Fermi level as well. Consequently, E_C takes a negative value for degenerately doped semiconductors.

The condition $Ln_D < Q_t$ describes a situation of only partially filled traps and grains that are completely depleted of electrons. For $Ln_D > Q_t$, the traps are completely filled with electrons and the grains are partially depleted. Neglecting the n dependence of the Fermi level, one sees from Eqs. (7a) and (7b) that E_B first increases linearly with n_D, reaches a maximum at $Ln_D = Q_t$, and then decreases as $1/n_D$. The highly doped semiconductors investigated in this work all fulfill the condition $Ln_D \gg Q_t$. Then, the convenient assumption $n_D \approx n$ is justified.

Figure 2 illustrates three possible transport paths across such potential barriers at grain boundaries: thermionic emission, thermionic field emission, and field emission [39]. We show in Sec. III that field emission is the dominant transport path across grain boundaries in highly doped polycrystalline films investigated in this contribution. In anticipation of this result, we focus on field emission in the following. Nevertheless, since thermionic emission is the transport path most often used in order to describe grain-boundary scattering in highly doped semiconductors, a comprehensive and critical review of this mechanism is presented in Appendix B. Furthermore, we detail a

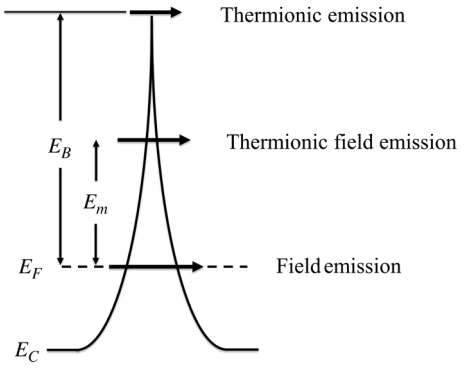

FIG. 2. A potential barrier at a grain boundary in degenerate semiconductors is illustrated. E_C and E_F denote the energy level of the conduction band and the Fermi level, respectively. The Fermi level lies within the conduction band. E_B measures the barrier height from the Fermi level to the top of the barrier. Electrons can pass the potential barrier by thermionic emission over the barrier, by thermally activated tunneling (thermionic field emission) at the energy E_m, and by tunneling (field emission) at the Fermi level.

description of thermionic field emission in Appendix D. In a final step, we review criteria that reveal which of the three transport processes across grain boundaries dominate for a given material.

1. Field emission

Field emission is the quantum-mechanical tunneling of electrons through thin potential barriers. Field emission is considered by several authors to be an important transport path across grain boundaries in polycrystalline materials [34,36,40–44]. Therein, if any, expressions of Holm [45] or Simmons [46] have been used. Holm's equation predicts temperature-independent field-emission currents. As Stratton and Simmons obtain a slightly quadratic dependence of the current on the temperature, Holm's equation is not considered further [11,47].

To our knowledge, the only publication that implements an analytical field-emission model is the one by Garcia-Cuenca, Morenza, and Esteve [43]. They use the expressions derived by Simmons to explain temperature-dependent conductivity measurements of CdS:In films [46]. However, the Simmons formula takes into account only the averaged barrier height. It is, in a manner of speaking, blind for the actual shape of the barrier. Consequently, his model does not contain thermionic field emission.

In this work, we adapt equations derived by Stratton [11,12]. Stratton's equations include the specific barrier shape and deal explicitly with thermionic field emission.

The field-emission current

$$J_{\mathrm{FE}} = e\frac{4\pi m^*}{h^3}\int_0^\infty \left[[f_1(E) - f_2(E)]\int_0^E P(E_x)dE_x\right]dE \tag{8}$$

is given by the integral of the difference between the two Fermi Dirac function f_1 and f_2 at each side of the barrier multiplied with the integral over the tunneling probability $P(E_x)$ at the electron's energy E_x. $P(E_x)$ may be computed using the WKB approximation [48,49] by

$$P(E_x) = \exp\left\{-\frac{2}{3}\frac{(E_B - E_x)^{3/2}}{E_{00}\sqrt{\phi_B}}\right\} \tag{9}$$

with E_B and ϕ_B being the barrier height measured with respect to the Fermi level and the conduction band, respectively [50]. E_{00} is defined as

$$E_{00} = \frac{2e}{\alpha}\sqrt{\frac{n}{2\epsilon_0\epsilon_r}} = \frac{\hbar}{2}\sqrt{\frac{n}{\epsilon_0\epsilon_r m^*}}, \tag{10}$$

where $\alpha = 2(2m^*)^{1/2}/\hbar$ is a constant. Under the assumption that predominantly electrons close to the Fermi level contribute to the current,

$$P(E_x) \approx \exp\{-(b_1 + c_1\epsilon_x + f_1\epsilon_x^2)\} \tag{11}$$

can be expanded with respect to the variable $\epsilon_x = E_F - E_x$. The computation of the tunneling coefficients b_1, c_1, and f_1 for double Schottky barriers at grain boundaries may be found in Appendix C. Here, just the results

$$b_1 = 2\frac{E_F}{E_{00}}\left[\sqrt{\tilde{E}^2 + \tilde{E}} - \ln\left(\sqrt{\tilde{E}+1} + \sqrt{\tilde{E}}\right)\right], \tag{12}$$

$$c_1 = 2\frac{1}{E_{00}}\ln\left(\sqrt{\tilde{E}+1} + \sqrt{\tilde{E}}\right), \tag{13}$$

$$f_1 = 2\frac{1}{4E_{00}E_F}\sqrt{\frac{\tilde{E}}{\tilde{E}+1}} \tag{14}$$

are presented. The parameter $\tilde{E}$ is given by

$$\tilde{E} = \frac{E_B - \mathrm{eV}}{E_F}. \tag{15}$$

Note the difference between the expression of f_1 as presented here and as given by Padovani [51]. A short discussion regarding this difference can be found in Appendix C.

The combination of Eqs. (8) and (11) and the evaluation of b_1 and c_1 for small applied voltages V yields the $J - V$ characteristic given by Padovani [51]:

$$J_{\mathrm{FE}} = \frac{A^*\exp(-b_1)}{(c_1k_B)^2}\left\{\left(\frac{\pi c_1 k_B T}{\sin(\pi c_1 k_B T)}[1 - \exp(-c_1\mathrm{eV})]\right) - c_1\mathrm{eV}\exp(-c_1E_F)\right\} \tag{16}$$

with $A^* = 4\pi m^* e k_B^2/h^3$ being the Richardson constant. Using the relation

$$\sigma = L\left.\frac{dJ}{dV}\right|_{V=0}, \tag{17}$$

we obtain for the field-emission conductivity σ_{FE} in polycrystalline semiconductors the expression

$$\sigma_{\mathrm{FE}} = \frac{eLA^* c_1}{(c_1 k_B)^2}\exp(-b_1)\left\{\frac{\pi c_1 k_B T}{\sin(\pi c_1 k_B T)} - \exp(-c_1 E_F)\right\}. \tag{18}$$

The same formula is derived by Yu with the exception that his expression already contains the relation $c_1 = E_B/E_{00}$ deduced from Eq. (13) for $V \approx 0$ [52]. The variation of mobility with temperature as derived from Eq. (18) is shown in Fig. 3. We assume the charge-carrier density to be constant. The temperature dependence of

$$\sigma_{\mathrm{FE}} \sim \frac{\pi c_1 k_B T}{\sin(\pi c_1 k_B T)} \approx 1 + \frac{1}{6}(\pi c_1 k_B T)^2 \tag{19}$$

is approximately quadratic. For representative values of n, L, and Q_t, this quadratic dependence translates into a charge-carrier mobility that is almost constant for low temperatures up to 100 K. Higher temperatures induce a slight mobility increase. The trap density hardly influences the general shape of the curve. However, it strongly determines the overall mobility level.

Note that a potentially nonparabolic conduction band is considered by the use of n-dependent effective mass m^* [see Eq. (5) in Sec. II A] and Fermi level E_F [see Eq. (5) in

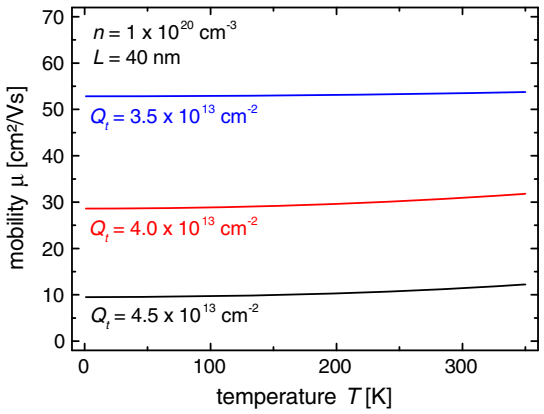

FIG. 3. The temperature-dependent mobility μ is plotted for three different trap densities Q_t. A constant carrier concentration of 1×10^{20} cm^{-3} and a grain size of 40 nm are assumed. The mobility is almost constant for temperatures up to 100 K and increases approximately quadratic for higher temperatures. Note that the trap density influences predominantly the overall level of the mobility and not so much the general shape of the curve.

Ref. [26]]. However, we do not use Stratton's extended theory for nonparabolic energy bands, because he claims it to be important only if the ratio E_B/E_g is large, which it is not in our cases.

Equation (18) describes tunneling through barriers with a uniform height. However, fluctuating barriers might be a better description of the real system [50]. Also, thermionic emission theory comprises extensions that take into account fluctuating barriers (see Appendix B). However, the derivation of an analytical expression for tunneling through fluctuating barriers needs strong simplifying assumptions (see Appendix E). These simplifications predominate the benefits of the more detailed barrier description. Therefore, Eq. (18) is the expression of choice for tunneling through potential barriers at grain boundaries.

Of course, a numerical solution for the expression of field emission through fluctuating barriers would be possible. However, it is our aim in this work to rely on analytical expressions.

2. *Which process dominates the transport across grain boundaries?—Criteria*

Depending on the doping concentration and temperature, one of the three transport paths across grain boundaries dominates. Crowell and Rideout [53] and Stratton [11,12] have developed criteria revealing the dominant transport mechanism.

Crowell and Rideout's criterion is based on the parameter $k_B T/E_{00}$. Following Rhoderick and Williams, E_{00} can be interpreted as the barrier height, measured relative to the conduction band, such that an electron at the bottom of the conduction band and at the edge of the depletion region has the field-emission probability equal to $\exp(-1)$. "Therefore the ratio $k_B T/E_{00}$ is a measure of the relative importance of thermionic emission and tunneling. As a rough guide, we should expect field emission if $k_B T \ll E_{00}$, thermionic field emission if $k_B T \approx E_{00}$, and thermionic emission if $k_B T \gg E_{00}$" [50].

More exact criteria have been given by Stratton [11,12]. Field emission occurs if the inequality

$$1 > k_B T(c_1 + \sqrt{2 f_1}) \tag{20}$$

is fulfilled. If the inequalities

$$1 < c_1 k_B T \tag{21}$$

$$\text{and} \quad 1 < b_m + c_m(E_F - E_m) + f_m(E_F - E_m)^2 \tag{22}$$

are complied with, the process is described by thermionic field emission. The criterion for thermionic emission is given by

$$1 > b_m + c_m(E_F - E_m) + f_m(E_F - E_m)^2. \tag{23}$$

III. APPLICATION AND EVALUATION

The application of the conductivity model developed in Sec. II is presented below. Mobility and conductivity data from the literature and our own experiments are investigated as a function of charge-carrier concentration n and measurement temperature T. The observed dependencies are fitted taking into account ionized-impurity, electron-phonon, and grain-boundary scattering.

The charge transport across potential barriers at grain boundaries comprises three mechanisms: field emission, thermionic field emission, and thermionic emission. Criteria to decide on the dominant transport path are given in Sec. II C 2. As the highest measurement temperature is generally 300 K, and as the lowest carrier concentrations are around 5×10^{19} cm^{-3}, Crowell and Rideout's criterion

$$k_B T \approx 25 \text{ meV} < 88 \text{ meV} = E_{00} \tag{24}$$

suggests field emission to be the dominant transport path for all investigated samples. This hypothesis is checked and verified for each fit by evaluating Stratton's more detailed criteria with the obtained barrier heights. Thus, for the highly doped polycrystalline semiconductors under investigation in this work, it is certain to state the important result that *field emission is the dominant transport path across grain boundaries.*

Altogether, the conductivity model consists of ionized-impurity scattering (ii), electron-phonon scattering (ph), and field emission at grain boundaries (FE). The three scattering mechanisms are combined using Matthiessen's rule. It states that the total resistivity

$$\rho_{\text{tt}} = \rho_{\text{ii}}(n, K) + \rho_{\text{ph}}(n, T, \Theta, \lambda_{\text{tr}}) + \rho_{\text{FE}}(n, T, Q_t, L) \tag{25}$$

is the sum of the resistivities of the individual scattering mechanisms. Three fit parameters occur: Debye temperature Θ, electron-phonon coupling constant λ_{tr}, and grain-boundary trap density Q_t. If not otherwise stated, a compensation ratio of $K = 0\%$ and a grain size of $L = 40$ nm [54,55] are assumed. Note that ρ_{ph} is a function of n, whereas μ_{ph} is independent of n (see Sec. II B).

A. Mobility as a function of carrier concentration

Within the presented conductivity model, the mobility μ depends among others on the carrier concentration n. It is shown that the model can fit the observed μ-n dependencies. The only fit parameter is the grain-boundary trap density Q_t, because electron-phonon scattering cannot be extracted from μ-n data. Anticipating results of μ-T fits, one estimates reasonable values for Θ and λ_{tr} to be 1000 K and 0.3, respectively, resulting in an electron-phonon scattering mobility of 200 cm^2/V s. Note that this value is similar to 210 cm^2/V s derived by Ellmer [21].

Figure 4 shows the mobility data of ZnO:Al films obtained by Berginski *et al.* [56] and Sommer *et al.* [57]. By varying the target doping concentration (TDC) and deposition temperature, samples with various carrier concentrations and mobilities are obtained [56]. Additionally, Fig. 4 shows the data of a seed-layer concept (red asterisk). This concept is based on the utilization of a thin seed layer with TDC = 2 wt % that improves the electrical properties, and, in particular, the mobility, of a subsequently grown bulk layer with TDC = 1 wt %. Further details about the seed-layer concept can be found in Ref. [57].

In a first approach, the data are modeled with the conductivity model assuming a trap density that is i ndependent of the carrier concentration (dashed lines). They fit the samples with TDC of 0.2 and 0.5 wt % and the seed-layer data reasonably well. Layers with TDC of 1 and 2 wt %, however, are not well described. A second approach is inspired by results in CdS:In [43] and silicon [44], where the trap density is found to be dependent on the carrier concentration. Thus, the trap density Q_t is assumed to be linked to the carrier concentration by the most simple functional dependence, that is, a linear relationship. The obtained relation

$$Q_t = Q_t(n) = Q_{t0} + C_t n \tag{26}$$

contains two unknown parameters Q_{t0} and C_t that are used to fit the data in Fig. 4 again. C_t is restrictively assumed to be the same for all TDCs. The fit results, shown as solid lines in Fig. 4, reproduce the data very well. Only the seed layer is still described best by the model without an n-dependent trap density. Hence, the seed-layer approach

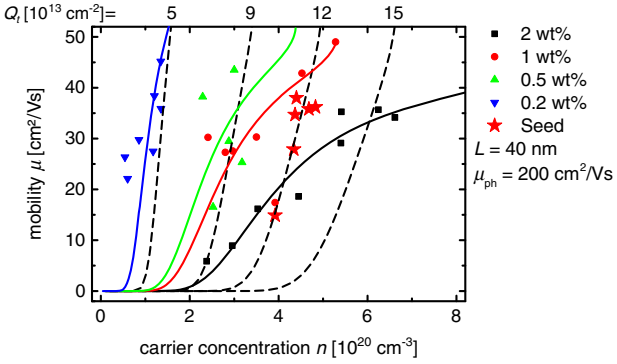

FIG. 4. The mobility is plotted against the carrier concentration for four different target doping concentrations. The data are extracted from Ref. [56]. Furthermore, the data of a seed-layer approach are added [57]. Dashed lines represent the results of the conductivity model assuming the trap density to be independent of the carrier concentration. Four different grain-boundary trap densities are evaluated: $Q_t = 5,\ 9,\ 12,\ 15 \times 10^{13}$ cm^{-2}. Solid lines show the fits under the assumption of a trap density being dependent on the carrier concentration.

TABLE I. Parameters of fits to data in Fig. 4 according to Eq. (26).

TDC (wt %)	0.2	0.5	1	2
Q_{t0} (cm^{-2})	2.7×10^{13}	4.4×10^{13}	4.8×10^{13}	6.0×10^{13}
C_t (cm)		1.5×10^{-7}		

seems to enable the increase of carrier concentration without affecting the grain-boundary trap density.

The fit parameters in Table I show an increase of Q_{t0} with increasing TDC. The dopant aluminum might thus be an important factor for the traps at the grain boundaries as also suggested by other authors [58]. A qualitative explanation for the n-dependent trap density is given in Sec. III B 2.

Figure 5 shows data that are extracted from Ref. [59]. The reasonable fit is based on the assumption of n-dependent trap densities at the grain boundaries. It reproduces both the mobility increase of ZnO (blue triangles) and the mobility decrease of ZnO:Al (red circles) with increasing carrier concentration.

The mobility increase of ZnO is easily explained by the increasing field emission through grain boundaries at higher carrier concentrations. The mobility decrease of ZnO:Al can be accounted for by two effects: (i) The effective mass increases with increasing carrier concentration due to the nonparabolic ZnO conduction band. As a consequence, the mobility as determined by

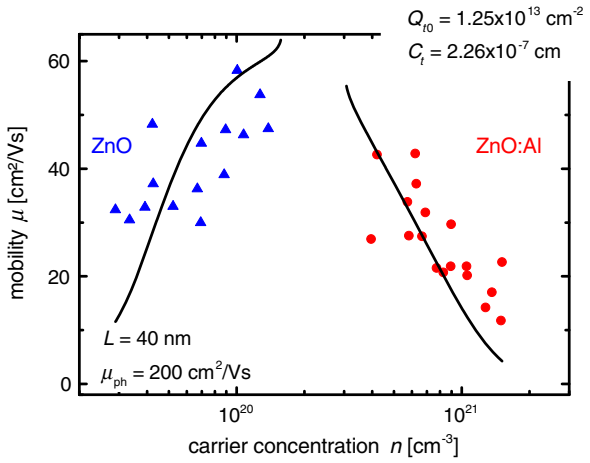

FIG. 5. The mobility is shown as a function of the carrier concentration for intrinsic (blue triangles) and aluminum-doped (red circles) ZnO. The data are extracted from Ref. [59]. The black solid line represents a fit with the conductivity model assuming a grain-boundary trap density that is dependent on the carrier concentration according to Eq. (26). The fit parameters Q_{t0} and C_t are given in the graph. The fit represents the increasing mobility for ZnO and the decreasing mobility for ZnO:Al. The fit is not a continuous line, because the Fermi level is situated above the potential barriers at grain boundaries for 1.5×10^{20} $cm^{-3} < n < 3.1 \times 10^{20}$ cm^{-3}.

ionized-impurity scattering decreases. Minami *et al.* explain their data in this way. However, Ellmer pointed out that Minami's effective mass of $m^* = 1.04m_e$ at $n = 1 \times 10^{21}$ cm^{-3} is rather high and possibly problematic [21]. In our case, a lower effective mass is used. Thus, only a part of the mobility decrease can be explained, and a further explanation is needed. (ii) Higher carrier concentrations need to induce an increasing barrier height at the grain boundaries to explain the reduction of mobility due to the field emission of electrons through grain boundaries. This would be the case if the number of additional traps induced by the higher carrier concentration is high, i.e., C_t is high. Such a situation is predicted by the fit in Fig. 5. Hence, the specific energetic distribution of the traps at grain boundaries in conjunction with the field-emission model might explain the mobility drop at high carrier concentrations.

B. Mobility as a function of measurement temperature

Electron-phonon scattering and field emission through grain boundaries are dependent on temperature. Thus, the evaluation of the proposed conductivity model has to comprise the investigation of temperature-dependent conductivity measurements. In total, five different measurement series are analyzed.

1. Fits to literature data

First, indium-doped cadmium sulfide (CdS:In) films are discussed, because their conductivity has been interpreted in terms of a different field-emission model than the one used here [43]. Most importantly, these films exemplify the importance of electron-phonon scattering for the interpretation of conductivity data. Furthermore, sputtered ZnO:Al and LPCVD-grown ZnO:B with various carrier concentrations are investigated. They underline that different dopants, grain sizes, and growth methods do not alter the applicability of the model. At the end, damp-heat-degraded ZnO:Al is discussed, because damp-heat degradation is supposed to predominantly influence grain boundaries. Therefore, it is an interesting system for the application of the field-emission model.

Figure 6 shows temperature-dependent conductivity measurements of CdS:In films. The data are obtained from Garcia-Cuenca, Morenza, and Esteve [43]. Garcia-Cuenca, Morenza, and Esteve propose a conductivity model comprising field emission through grain boundaries to interpret their data. The field-emission model is based on the description of Simmons [46], whereas the model developed here uses the equations of Stratton [11,12]. Generally, the two models yield similar results, because both models predict an approximately quadratic temperature dependence. Garcia-Cuenca, Morenza, and Esteve use the expression $\sigma = \sigma_0(1 + \beta T^2)$ as a fit function. Fit parameters are σ_0 and β. Both parameters are essentially a

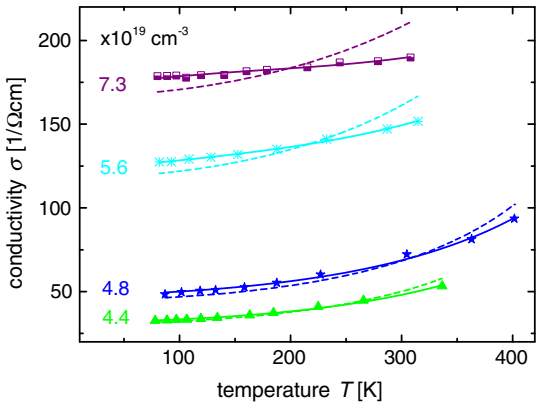

FIG. 6. Temperature-dependent conductivity measurements of polycrystalline CdS:In films with various carrier concentrations are shown. The data are obtained from Garcia-Cuenca, Morenza, and Esteve [43]. The dashed lines are fits taking into account our field-emission model at grain boundaries only. The solid lines are fits applying our field-emission model and electron-phonon scattering. The same fits (solid lines) can be obtained by using the field-emission model of Garcia-Cuenca, Morenza, and Esteve. Note that a parabolic conduction band is assumed. Garcia-Cuenca, Morenza, and Esteve specify a grain size of 500 nm.

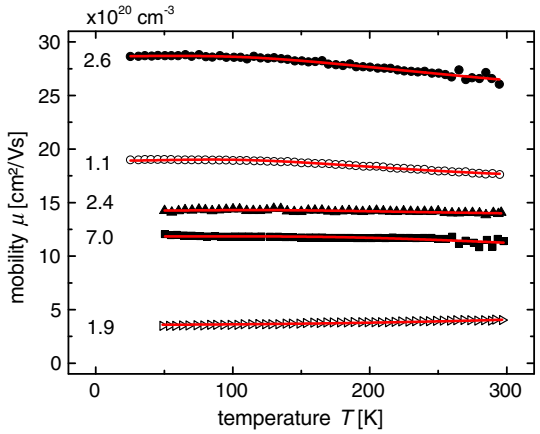

FIG. 7. The mobility of sputtered polycrystalline ZnO:Al is measured as a function of the temperature. Films with various carrier concentrations are investigated. The data are extracted from Ellmer and Mientus [60]. Red lines represent fits comprising uncompensated ionized-impurity scattering, electron-phonon scattering, and field emission through grain boundaries. Fit parameters are Θ, λ_{tr}, and Q_t. No information is given by Ellmer and Mientus about the grain size. Therefore, it is assumed to be 40 nm.

function of the trap density Q_t. We reproduce the fits of Garcia-Cuenca, Morenza, and Esteve (solid lines in Fig. 6) and obtain excellent results. However, similar to Garcia-Cuenca, Morenza, and Esteve, we are not able to reproduce the data such that σ_0 and β yield the same Q_t. In contrast, our model combining Stratton's field-emission theory in conjunction with additional electron-phonon scattering yields one unique Q_t. Furthermore, the fit curves obtained by our model cannot be distinguished from the ones using Garcia-Cuenca's model. Note that Stratton's field-emission model alone does not yield satisfying fits (dashed lines in Fig. 6).

Garcia-Cuenca, Morenza, and Esteve speculate that Q_t might be temperature dependent. Since this temperature dependence is not reflected in their model, the ambiguous Q_t values occur. The comparison of our model and the model of Garcia-Cuenca, Morenza, and Esteve hence reduces to the question whether Q_t is temperature dependent or electron-phonon scattering is significant. Further down in this paper, we cite data that undoubtedly show electron-phonon scattering. Since Garcia-Cuenca's approach yields ambiguous values for Q_t and Stratton's field-emission model alone does not yield satisfying fits, we stress the important result that *only the combination of field emission and electron-phonon scattering leads in most cases to a satisfying description of temperature-dependent conductivity data.*

Figure 7 shows mobility measurements of sputtered, polycrystalline ZnO:Al as a function of the temperature. The data are obtained by Ellmer and Mientus [60]. The samples possess different carrier concentrations. Although the grain size is unknown and thus a representative value for ZnO:Al of 40 nm is used, excellent fits are obtained. Some samples show a slight mobility increase at higher temperatures, whereas for others a mobility decrease is observed. In the framework of the proposed conductivity model, the positive and negative slope correspond to field emission and electron-phonon scattering, respectively. Field emission dominates the temperature behavior in the low-mobility film. In fact, the best fit for this sample is obtained by neglecting electron-phonon scattering. In contrast, the two samples with the highest mobility showed a temperature dependence that is dominated by electron-phonon scattering. The two other samples possess an almost constant mobility. Here, the temperature dependence of field emission and electron-phonon scattering compensate each other.

We state at the beginning of Sec. III that the total resistivity is obtained by the combination of three scattering mechanisms: ionized-impurity scattering (ii), electron-phonon scattering (ph), and grain-boundary scattering represented by the field-emission model (FE). Of course, not only the total resistivity but also the total mobility can be computed as a combination of the individual scattering mechanisms.

The three scattering processes are plotted separately in Fig. 8. Note that similar plots with similar conclusions can also be derived for the other data. It is clearly illustrated that the limiting mechanism is field emission through grain boundaries, because field emission shows the lowest mobility. The slight temperature dependence of field emission is hidden in the strongly temperature-dependent

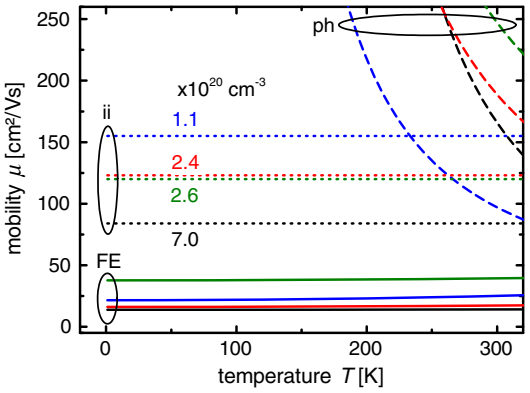

FIG. 8. Fits to data obtained from Ellmer and Mientus [60] shown in Fig. 7 are split into the three scattering mechanisms contained within the model, which are ionized-impurity scattering (ii), electron-phonon scattering (ph), and field emission at grain boundaries (FE).

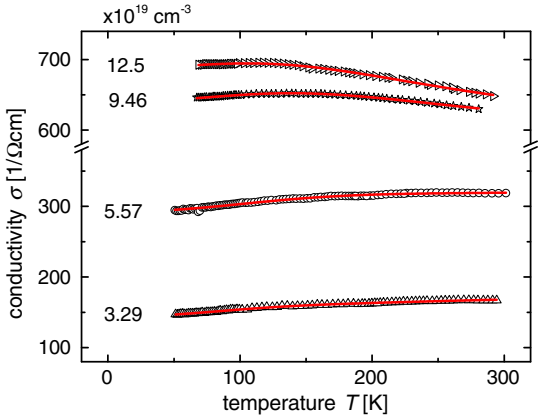

FIG. 9. The conductivity of polycrystalline ZnO:B was measured at various temperatures. The films have been grown by LPCVD. The carrier concentration is changed by varying the flow of the dopant precursor during deposition. The data are taken from Ref. [61]. Red lines are fits according to the conductivity model under investigation. Myong *et al.* obtain grain sizes of around 330 nm by SEM measurements.

electron-phonon scattering. Thus, it seems as if the mobility is, apart from electron-phonon scattering, temperature independent, although the slightly temperature-dependent field emission is limiting the overall mobility.

The above outlined argumentation focusing on grain-boundary scattering is not unambiguous due to its assumption of vanishing compensation. A different argumentation could assume grain-boundary scattering to be negligible. Consequently, the low mobility would be induced solely by ionized-impurity scattering that is amplified by compensation. Under this assumption, fits of most of the temperature-dependent measurements would also be possible.

Exemplarily, the mobility of the sample with $n = 1.1 \times 10^{20}$ cm^{-3} could be limited by ionized-impurity scattering if a compensation ratio of $K = 30\%$ is assumed. Note that, within our model, $K = 30\%$ means that 60% of the electrons, that have been provided by extrinsic donors, are absorbed by acceptors. Look *et al.* determine by SIMS measurements and positron annihilation spectroscopy a maximum compensation value of $K = 12\%$ in a ZnO:Ga film with $n = 12.8 \times 10^{20}$ cm^{-3}. Without having a clear proof, it is reasonable to suppose the compensation to increase with increasing dopant concentration. A value of $K = 30\%$ seems under this assumption high. Furthermore, the positive slope of the sample with $n = 1.9 \times 10^{20}$ cm^{-3} cannot be explained without an additional scattering mechanism, because ionized-impurity scattering is temperature independent. This additional mechanism is likely grain-boundary scattering. Hence, field emission is the mechanism to apply following the criteria derived in Sec. II C 2.

The data of Ellmer *et al.* contain only one sample showing the upwardly bent mobility curve that is characteristic for field emission. Temperature-dependent conductivity measurements extracted from Myong *et al.* are shown in Fig. 9. Their data contain more samples with a positive slope indicating field emission [61]. Both low-conductivity samples show a positive slope, i.e., increasing conductivity with increasing temperature. The sample with $n = 9.46 \times 10^{19}$ cm^{-3} illustrates nicely both effects, field emission at grain boundaries and electron-phonon scattering. A positive slope in the low-temperature range is observed that corresponds to field emission, and a negative slope in the high-temperature range is observed that corresponds to electron-phonon scattering. Evaluating the shares of the three scattering mechanisms shows field emission to be the limiting mechanism in these samples.

Temperature-dependent measurements of damp-heat-treated ZnO:Al films are presented by Kim *et al.* [62]. Their data are shown in Fig. 10. Damp-heat treatment degrades mobility and carrier concentration of doped ZnO [63–66]. Agreement exists in the literature that damp-heat degradation affects predominantly grain boundaries. Figure 10 shows the temperature dependence to be dominated by electron-phonon scattering, because only downwardly bent curves are observed. However, according to the proposed model, the overall mobility level is defined by field emission at grain boundaries. Indeed, the expected results of increased barrier height with increasing damp-heat time are obtained. The field-emission model thus agrees with the literature conception of damp-heat degradation.

Kim *et al.* use the Seto model to fit their data. Here, we also apply the Seto model and obtain the dashed line in Fig. 10. In contrast to Kim *et al.*, we extend the fit to temperatures below the lowest measurement temperature, and we do not use an Arrhenius plot. As a result, one observes clearly that the agreement between the fit and measurement is poor. Note especially that the Seto fit

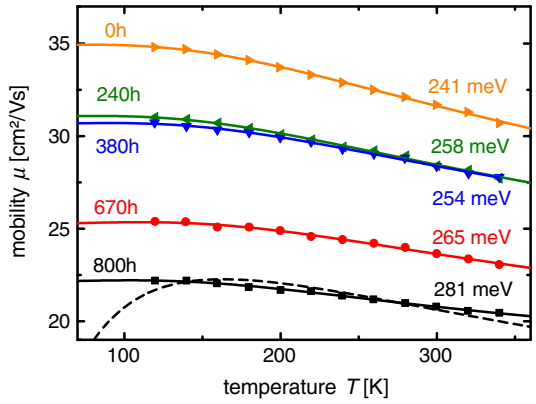

FIG. 10. The mobility of ZnO:Al films is measured at temperatures from 100 to 350 K. The investigated films have undergone damp-heat treatments for various durations. The data are taken from Ref. [62]. The measurements are fitted with the proposed conductivity model. The barrier heights deduced from the model are given in the graph. The dashed line is a fit according to the Seto model. Kim *et al.* give a grain size of 75 nm.

predicts a rather improbable mobility decrease at low temperatures.

Figure 11 shows the temperature-dependent conductivity of samples that have been investigated in the framework of a seed-layer concept. This concept is mentioned in Sec. III A. Details about the approach can be found in Sommer *et al.* [57]. Here, it is important only that the application of a 40-nm-thin seed layer improves the mobility of the 800-nm-thick total layer significantly. Figure 11(a) reveals conductivity measurements of samples with (squares) and without (circles) a seed layer. The measurement temperature is varied from 90 to 330 K. Solid and dashed lines represent fits using the proposed conductivity model.

The temperature dependence of the sample with a seed layer is dominated by electron-phonon scattering, although the overall conductivity level is still determined by grain-boundary scattering. In contrast, the sample without a seed layer could be fitted using the field-emission model only. Thus, the increased conductivity of the seed-layer sample in comparison to the sample without a seed layer is due to a significant reduction of grain-boundary scattering.

The sample without a seed layer provides an interesting feature that is observed when the conductivity is depicted as a function of the squared measurement temperature. The field-emission model exhibits a quadratic temperature dependence. Therefore, one should observe a single straight line in Fig. 11(b). However, not a single but two straight lines with different slopes are observed. The fit, depicted as the red dashed line, is an average of both slopes. It agrees well with the smaller slope, since the smaller slope dominates over a wide temperature range. Such measurements showing two straight lines are also reported for polycrystalline silicon films [44]. The observation is explained by disorder in the films, i.e., nonuniform barrier heights and dopant distribution.

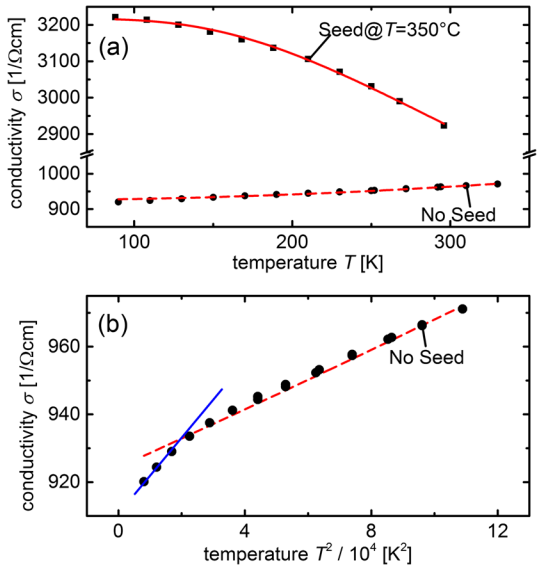

FIG. 11. Temperature-dependent conductivity measurements: (a) Samples with (squares) and without a seed layer (circles) are investigated. Red lines are fits using the conductivity model under investigation. Note that the sample without a seed layer is fitted using the field-emission model only. (b) The conductivity of the sample without a seed layer is plotted over the squared temperature. The red dashed line represents the fit also shown in (a). However, two different slopes are present in the measurement. The blue solid line is a guide to the eye for the steeper slope.

2. *Analysis of fit parameters*

Fit parameters of the investigated measurement series are evaluated regarding their consistency and their implications for the trap distribution at grain boundaries.

The field-emission model contains one fit parameter: the grain-boundary trap density Q_t. Various Q_t values extracted from fits of temperature-dependent measurements are plotted in Fig. 12(a) as a function of carrier concentration n. One observes that the trap density increases with increasing carrier concentration. Note again that the Q_t values are obtained from fits of temperature-dependent measurements. Let us shortly remind you of the fits to μ-n data. There, satisfying fits can be obtained only under the assumption of a trap density that depends on the carrier concentration. A simple linear relation between Q_t and n with the parameters Q_{t0} and C_t is proposed [see Eq. (26)]. The same linear relationship is used to fit the Q_t-n dependence that is obtained from various temperature-dependent measurements. The dashed line in Fig. 12(a) represents this fit. The agreement between the experimental data and fit is reasonable. Note that the carrier concentration is given on a logarithmic scale. The values for Q_{t0} and C_t obtained from the fit to temperature-dependent measurements are similar to the values obtained by the fitting of μ-n data (see Table I). Thus, the results of μ-n and μ-T data are consistent. Both reveal an increasing trap density at the grain boundaries with increasing carrier concentration.

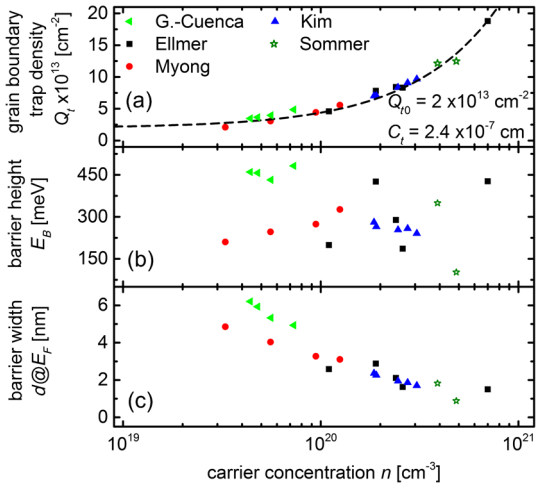

FIG. 12. (a) The grain-boundary trap density Q_t is shown as a function of the carrier concentration. The dashed line is a fit according to Eq. (26). The fit parameters Q_{t0} and C_t are presented. Note that the CdS:In films of Garcia-Cuenca, Morenza, and Esteve are not included into the fit. From Q_t, one can derive the barrier height E_B (b) and the barrier width d at the Fermi level (c).

The fits to μ-n data of Berginski *et al.* show that different TDCs need different values for Q_{t0} to fit the μ-n data (see Fig. 4 and Table I). The increase of TDC might thus induce more traps. Trap states at grain boundaries might originate from two different sources. First, grain boundaries can be viewed as internal interfaces of adjacent grains. Thus, interface states might exist due to the disturbance of the regular crystalline order. These interface states are either intrinsic or extrinsic [67]. Extrinsic interface states might be induced by, e.g., water vapor. As a result, the conductivity of ZnO:Al decreases under damp-heat treatment [63,66,68,69]. Second, impurities could segregate at grain boundaries whereby defects occur that trap electrons. A major impurity in highly doped semiconductors is the dopant. Therefore, the dopant aluminum is supposed to be a cause for trap states at grain boundaries in ZnO:Al [58]. In our case, Q_{t0} increases with increasing TDC. This result suggests that mainly deep traps are affected by the dopant aluminum [70]. However, it is not a clear verification of the trap states' origin. Further insights into the real origin of trap states might be possible by the use of experiments that provide resolution on the atomic scale such as atom probe tomography [71].

The n-dependent trap density may be explained by two different effects. First, the increase of carrier concentration could correspond to an increase of impurities, i.e., dopant atoms, at the grain boundaries. Deposition conditions may alter the concentration of dopant atoms. For instance, the increase of deposition temperature leads to an increase of aluminum concentration in ZnO:Al due to a favored reevaporation and resputtering of zinc in comparison to aluminum [57]. The increasing dopant concentration thus induces a higher density of trap states and a higher carrier concentration. Second, the n-dependent trap density might be caused by the energetic distribution of trap states. Figure 13 illustrates the hypothesis of trap states being distributed in energy. Only the trap states with energies equal to or below the Fermi level are occupied. The increase of carrier concentration induces a rising Fermi level. Consequently, trap states that were formerly unoccupied can now be filled with electrons, and the density of occupied traps is boosted. This hypothesis is supported by scanning tunneling measurements of ZnO:Al [72]. They reveal that trap states are broadly distributed in energy and that trap states above the Fermi level exist. Note that, in either scenario, the basis of trap states ($\sim Q_{t0}$) is created by the dopant and correlates with the TDC.

Figures 12(b) and 12(c) show the barrier height and width. Both parameters are derived from the occupied trap density. Note that the obtained barrier heights are one order of magnitude higher than the ones found in the literature. This is a direct result of the generally higher trap densities. Exemplarily, Ellmer and Mientus [14] give a maximum trap density of 3×10^{13} cm^{-2}. The barrier height (with respect to the Fermi level) varies more strongly than the trap density. The reason is that, first, the barrier height is calculated as the difference between the barrier height relative to the conduction band and the Fermi level and that, second, the barrier height with respect to the conduction band is a quadratic function of the trap density [see Eq. (7b)]. Thus, the quadratically varying minuend, i.e., the barrier height with respect to the conduction band, induces a strong variation of the barrier height relative to the Fermi level. The barrier height shows no correlation with the carrier concentration. In contrast, the barrier width at the Fermi level decreases slightly with increasing carrier concentration. The reason might be the higher barrier height measured with respect to the conduction band at higher carrier concentrations. Consequently, the barrier at the Fermi level can be narrower, although the barrier height

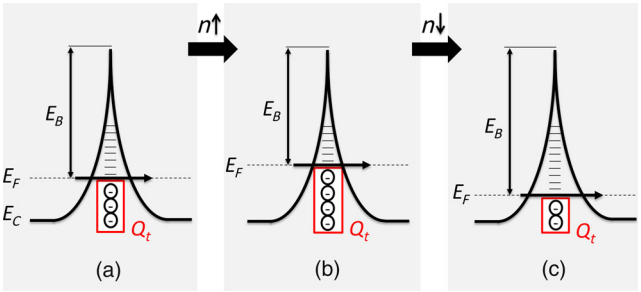

FIG. 13. Barriers at grain boundaries are created by charged traps. (a) Trap states at grain boundaries are energetically distributed. States below E_F are occupied and contribute to the trap density Q_t. (b) An increasing carrier concentration n is accompanied by an increase of the Fermi level. Thus, more traps can be filled and Q_t is raised. (c) If n decreases, the Fermi level drops and fewer traps are occupied.

given relative to the Fermi level might be the same. Generally, no correlation between either the barrier height or width and mobility is found. Only the combination of both barrier height and width determines the field-emission mobility.

Figure 14 depicts the fit parameters of electron-phonon scattering: electron-phonon coupling constant λ_{tr} and Debye temperature Θ. λ_{tr} varies between 0 and 0.6 with the exception of one ZnO:B sample and the CdS:In films, where values exceeding 0.6 are obtained. The results seem to be reasonable, because Allen obtains for metals values in the range of 0.5 [30]. Also, the determined values for Θ of 500 to 1500 K are similar to Allen's results. Debye temperatures of single-crystalline ZnO found in the literature ($\Theta = 370$ [73], 399.5 [74], 420 [75], and 920 K [76]) are similar to our results, although we derive slightly higher values. Our Θ for nanocrystalline CdS of 1000 K is higher than the one published by other authors ($\Theta = 300$ K [77]). On the one hand, the difference between our Θ values and those published in the literature may reflect the deficiency of the simple Bloch-Grüneisen model. On the other hand, it may hint at the strong influence of the polycrystalline structure on the Debye temperature.

In general, it would be desirable to derive the fit parameters by an alternative method such as *ab initio* calculations in order to get a truly predictive theory. However, the TCO's polycrystalline structure, and thus the quite dominant disorder in these materials, should make it very challenging to simulate them on an atomistic level. In addition, the structural and chemical nature of grain boundaries is far from being known. There are several experimental and theoretical studies to reveal the atomistic structure of grain boundaries in ZnO [41,78,79]. However, they focus on very specific grain boundaries with idealized geometry. In contrast, the nature of grain boundaries in the materials studied in this contribution is unknown. Various tilt angles, intrinsic defects, and foreign atoms like hydrogen or the dopant aluminium might form a broad ensemble of grain boundaries. Therefore, methods such as *ab initio* calculations might need strong assumptions with regard to the atomistic arrangement which would then prevent the calculation from being truly predictive.

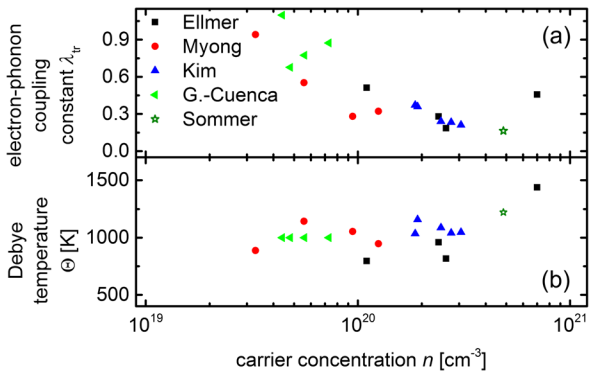

FIG. 14. Electron-phonon scattering contains two fit parameters. They are presented in this graph: (a) electron-phonon coupling constant λ_{tr} and (b) Debye temperature Θ.

IV. CONCLUSION

To further the understanding of electron-scattering mechanisms, we propose a conductivity model for highly doped polycrystalline materials that comprises ionized-impurity scattering, electron-phonon scattering, and field emission at grain boundaries. Ionized-impurity scattering, described by the theory of Brooks, Herring, and Dingle, and electron-phonon scattering, implemented by the Bloch-Grüneisen law, are both scattering mechanisms which are located within the grain. However, besides these well-known and accepted intragrain scattering mechanisms, scattering at grain boundaries is considered.

Grain boundaries induce defects that trap electrons, which results in potential barriers that scatter electrons. Electrons can pass these potential barriers by three different mechanisms: thermionic emission, thermionic field emission, and field emission. Thermionic emission, predominantly applied in the framework of the Seto model, is considered by the majority of authors as the dominant mechanism across potential barriers at grain boundaries. Field emission, also denoted as quantum-mechanical tunneling, and thermionic field emission are neglected in most cases. The progress made in this work is the adaptation of Stratton's analytical (thermionic) field-emission theory for the application to potential barriers at grain boundaries.

Criteria are presented that clearly identify field emission as the dominant transport mechanism through potential barriers at grain boundaries in highly doped semiconductors. In conjunction with the above outlined intragrain scattering mechanisms, excellent fits of temperature-dependent mobility and conductivity measurements are obtained. Materials under investigation are highly doped transparent conductive oxides with a special emphasis on ZnO:Al. We discover that only the combination of field emission and electron-phonon scattering leads to a satisfying description of the data. Also, mobility data, given as a function of the carrier concentration, are described satisfactorily. Merely three fit parameters, namely, the density of occupied traps at grain boundaries, the electron-phonon coupling constant, and the Debye temperature, have to be considered. The fit results suggest that the trap density at grain boundaries increases linearly with the carrier concentration.

We believe that our results offer perspectives and possibilities for the interpretation of mobility and conductivity data not only of TCOs but also of highly doped polycrystalline semiconductors, in general. The understanding of scattering mechanisms that limit the charge-carrier mobility in degenerately doped polycrystalline semiconductors is a step to improve the conductivity in these materials.

ACKNOWLEDGMENTS

We thank F. Ruske and D. Dorow-Gerspach for fruitful discussions. Financial support by the German Ministry BMWi (Contract No. 0325299) is gratefully acknowledged.

APPENDIX A: IONIZED-IMPURITY SCATTERING—MATERIAL PARAMETERS

Three material parameters are needed for the description of ionized-impurity scattering by Eq. (1). Here, we present our assessment of these parameters for ZnO:Al. However, the discussion may also serve as a guide for other materials.

1. Donor and acceptor charge $Z_{D,A}$

Two main doping mechanisms are discussed in the literature [21]. The first one is the doping by extrinsic dopants such as boron, aluminum, or gallium. These extrinsic dopants possess a charge of $Z_D = 1$. The second doping mechanism could be intrinsic doping by oxygen vacancies resulting in $Z_D = 2$. Look *et al.* show the main donor to be gallium in their ZnO:Ga films [32]. Furthermore, they identify Zn vacancies as the main acceptor, which is supported by theoretical investigations [80]. Thus, the further assumption in this work is $Z_D = 1$ (extrinsic doping by aluminum) and $Z_A = 2$ (Zn-vacancy acceptor). Note that this assumption implies, first, the neglect of ionized-impurity clusters and, second, a maximum compensation ratio of $K = 50\%$.

2. Compensation ratio K

The compensation ratio's impact on the mobility is shown in Fig. 15 for $K = 5\%$ and $K = 10\%$. Look *et al.* determine compensation ratios between 3% and 12% for ZnO:Ga films with carrier concentrations between 7.8×10^{20} and 12.8×10^{20} cm^{-3} [32,87]. If not otherwise stated, we assume a compensation ratio of $K = 0\%$.

3. Effective mass m^*

The effective mass is controversially discussed in the literature. Values of $m^* = 0.28m_e$ [68,88,89], $m^* = 0.34m_e$ [32], $m^* = 0.5m_e$ [42], and $m^* = 0.6m_e$ [90] may be found. Of course, these constant values implicitly assume a parabolic conduction band, i.e., the effective mass is independent of the carrier concentration. However, a more realistic description takes into account the nonparabolicity of the conduction band. As a consequence, the effective mass becomes dependent on the carrier concentration. This dependence is described by Eq. (5), which contains two free parameters, m_0^* and C, that need to be fixed. Figure 15 shows the mobility as a function of the carrier concentration for three different parameter sets of m_0^* and C. The mobility determined solely by ionized-impurity scattering for $K = 0\%$ should be an upper limit, because all other scattering mechanisms, that might further decrease the mobility, are neglected. For the as-grown layers (solid symbols) in Fig. 15, all three theoretical curves (solid lines) may represent this upper limit, because the experimental data do not exceed them. However, the annealed samples and the optically characterized as-grown films show mobility values close to or even slightly above the curve determined by parameters of Young and co-workers.

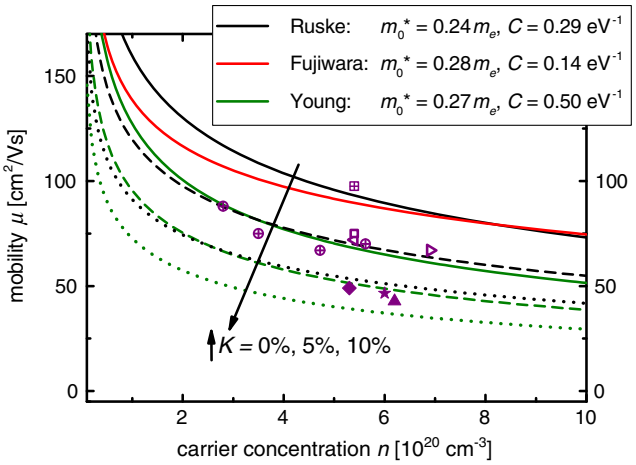

FIG. 15. The mobility limited by ionized-impurity scattering is computed as a function of the carrier concentration using Eq. (1). Three different parameter sets for the effective mass are evaluated: Ruske *et al.* [81] (black lines), Fujiwara and Kondo [82] (red lines), and Young *et al.* [83] (green lines). The parameters m_0^* and C are given in the graph. For Ruske *et al.* and Young *et al.*, the compensation ration K is varied from 0% (solid lines) to 5% (dashed lines) and 10% (dotted lines). Here, $Z_D = 1$ and $Z_A = 2$ are assumed. The experimental data are divided into as-grown layers (upward triangle [59], diamond [56], star [84]), as-grown layers whose mobility is determined by optical fits (⊕ [85]), layers annealed under a capping layer and measured at room temperature (open symbols: square [85], leftward triangle [86], rightward triangle [81]), and annealed samples measured at low temperatures to eliminate electron-phonon scattering (⊞ [85]).

The effect of electron-phonon scattering is eliminated by measuring the mobility at low temperatures. The value clearly exceeds the limit computed after Young and co-workers. Therefore, it is assumed that this parameter set overestimates the impact of ionized-impurity scattering. Both the parameter sets of Ruske *et al.* and Fujiwara and Kondo seem reasonable. They are obtained by fitting optical data. Ruske *et al.* use an extended Drude model, whereas Fujiwara and Kondo apply the classical Drude model. The extended Drude model is believed to be more appropriate for reasons outlined by Sommer [85]. The parameter set of Ruske *et al.* yields an effective mass of $0.35m_e$ for a carrier concentration of 5×10^{20} cm^{-3}. This value is close to $m^* = 0.34m_e$ determined by Look [32].

APPENDIX B: REVIEW ON THERMIONIC EMISSION

The thermionic emission theory across Schottky barriers is developed following Rhoderick and Williams [50] and subsequently applied to double Schottky barriers, i.e., grain boundaries.

The thermionic emission theory assumes the transfer of electrons over the barrier to be the dominant transport path across Schottky barriers. The concentration of electrons with energies larger than the barrier,

$$\tilde{n} = \int_{E_B}^{\infty} D(E) f(E,T,V) dE \approx N_c \exp\left\{-\frac{E_B - \mathrm{eV}}{k_B T}\right\}, \tag{B1}$$

is determined by the density of states $D(E)$ multiplied by the occupancy represented by the Fermi-Dirac function $f(E,T,V)$ and integrated for energies larger than the barrier. Using the Boltzmann approximation to the Fermi-Dirac function, $\tilde{n}$ may be expressed by the effective density of states $N_c = 2(2\pi m^* k_B T/h^2)^{3/2}$, the barrier height E_B, and the external applied voltage V. Further parameters are the electron charge e, the Boltzmann constant k_B, and the temperature T. Note that the Fermi level is taken to be the reference level at zero energy. The area density of electrons hitting the barrier per second is given by $\tilde{n}\,\bar{v}/4$. $\bar{v}$ is the average thermal velocity of electrons. Assuming a Maxwellian distribution of electron velocities, $\bar{v}$ can be computed as $\bar{v} = (8k_B T/\pi m^*)^{1/2}$. One further assumes that such electrons incident on the barrier are not reflected by, e.g., phonons. Moreover, one has to take into account the electrons flowing from the metal into the semiconductor. Then, the thermionic current J_{TE} across a Schottky barrier of height E_B is

$$J_{\mathrm{TE}} = \frac{e\bar{v}}{4} N_c \exp\left(-E_B/k_B T\right)\{\exp\left(\mathrm{eV}/k_B T\right) - 1\}. \tag{B2}$$

With the effective density of states N_c and the average thermal velocity $\bar{v}$, Eq. (B2) becomes the familiar relation

$$J_{\mathrm{TE}} = A^* T^2 \exp\left(-E_B/k_B T\right)\{\exp\left(\mathrm{eV}/k_B T\right) - 1\} \tag{B3}$$

containing the Richardson constant $A^* = 4\pi m^* e k_B^2/h^3$. The neglected effect of reflection at the barrier can be integrated into the model by modifying the Richardson constant [9]. The synthesis of thermionic and diffusion theory yields the relation $J = J_{\mathrm{TE}}/(1 + \bar{v}/v_D)$, where v_D is an effective diffusion velocity [91]. If $v_D \gg \bar{v}$, then $J \approx J_{\mathrm{TE}}$, and the thermionic emission theory applies. Orton shows the thermionic emission theory to be appropriate for polycrystalline materials [9,10].

Let us now apply the Schottky barrier theory to double Schottky barriers, that is, grain boundaries. As a consequence of the generally high number of grain boundaries within the material, one can assume the voltage drop across one grain boundary to be small [92]. Then, the grain-boundary limited conductivity σ of a polycrystalline material with grain size L can be computed using the relation

$$\sigma = \frac{L}{2}\left.\frac{dJ_{\mathrm{TE}}}{dV}\right|_{V=0}. \tag{B4}$$

The factor $1/2$ occurs because the voltage drops across two equal Schottky barriers [10,67]. The grain size L appears because the conductivity is after Matthiessen's rule proportional to the reciprocal number of grain boundaries #gb, i.e., $\sigma \sim 1/\#\mathrm{gb}$. As the number of grain boundaries equals furthermore the reciprocal grain size, it follows that $\sigma \sim [1/\#\mathrm{gb} = 1/(1/L) = L]$. Using Eq. (B3) in conjunction with the just-outlined modifications, the conductivity of a polycrystalline material is obtained by

$$\sigma_{\mathrm{TE}} = L\frac{eA^*}{2k_B} T \exp\left(-\frac{E_B}{k_B T}\right). \tag{B5}$$

Similar expressions are derived by Petritz [8] and Seto [7]. However, Seto uses Eq. (B2) in the form

$$J_{\mathrm{TE}} = \frac{e\bar{v}}{4}\overbrace{N_c \exp\left(-E_C/k_B T\right)}^{=n} \exp\left[-(E_B - E_C)/k_B T\right] \times \{\exp\left(\mathrm{eV}/k_B T\right) - 1\}, \tag{B6}$$

where E_C is the energy of the conduction band with respect to the Fermi level. The expression for the carrier concentration n is valid only for nondegenerate semiconductors, because it is based on Boltzmann statistics. Thus, Seto's model must not be applied to degenerate materials. For degenerate semiconductors, Eq. (B5) is appropriate given that $E_B \gg k_B T$. The conductivity derived by Seto,

$$\sigma_{\mathrm{TE}} = Ln\frac{e^2}{2\sqrt{2\pi m^* k_B}}\frac{1}{\sqrt{T}} \exp\left[-(E_B - E_C)/k_B T\right], \tag{B7}$$

and Eq. (B5) differ in their temperature dependence and in the exponent. Seto gives the barrier height relative to the conduction band, whereas the Schottky theory measures the barrier with respect to the Fermi level. Note that, similar to Eq. (B5), a factor of $1/2$ is also appended to Seto's equation.

A further assumption of the presented models is the uniform barrier height. Spatial fluctuations of Schottky barrier heights are introduced by Werner and Güttler to explain current-voltage and capacitance-voltage measurements [93]. Werner applies this model to grain boundaries

to elucidate curved Arrhenius plots as observed for many polycrystalline materials [94]. Werner assumes the barrier heights to have a Gaussian distribution $P(E_B)$ with a standard deviation $\tilde{\sigma}_B$ around a mean value $\bar{E}_B$. He includes the barrier fluctuations into the thermionic emission theory by performing an integration of the thermionic emission current described by Eq. (B3) over all potentials E_B. The application of fluctuating barriers to grain boundaries of polycrystalline materials yields

$$\sigma_{\mathrm{TE}} = L\frac{eA^*}{2k_B}T\exp\left\{-\frac{1}{k_BT}\left(\bar{E}_B - \frac{\tilde{\sigma}_B^2}{2k_BT}\right)\right\}. \tag{B8}$$

The fluctuating barriers induce a reduction of the effective barrier by $\tilde{\sigma}_B^2/2k_BT$. This reduction is more pronounced for lower temperatures, leading to the upwardly bent Arrhenius curves for high $1/T$ values. Several authors use the Werner model to fit data of polycrystalline materials [36,60,95]. However, some authors ignore the temperature dependence of the prefactor of the exponential function [36,60]. Others modify the Werner model according to the relation $N_c\exp(-E_C/k_BT) = n$, which is valid only for nondegenerate materials [95]. Nevertheless, such a model is applied to degenerate materials. We use the barrier heights derived from these questionable models, because other values are lacking.

Several authors claim the Seto or Werner model to be inaccurate for highly doped materials, because they do not take into account degeneracy [18,34,96,97]. In agreement with our conclusions, Bruneaux *et al.* state Eq. (B5) to apply to a degenerate electron gas and Seto's equation to a nondegenerate electron gas [97]. Zhang and Ma cite Bruneaux *et al.* but give a slightly different expression for the mobility in degenerate samples [34]. Explanatory remarks regarding their modification are not given by Zhang and Ma. Therefore, the expression used by Zhang and Ma is problematic as, e.g., pointed out by Liu *et al.* [33]. The expression is nevertheless used by other authors [18].

Kajikawa argues that the Boltzmann approximation is applicable only when the relation $E_c - E_F \gg k_BT$ holds [96]. Although this argument is certainly true in the case of the Seto model, it does not apply to Eq. (B5) and, thus, the Werner model. The criterion for the applicability of Boltzmann statistics with respect to thermionic emission at grain boundaries is $E_B \gg k_BT$. Only then are the approximation in Eq. (B1) and the expression for the average thermal velocity $\bar{v}$ valid. Values found in the literature for E_B are 0.3–8 [36], 3 [60], and 6.8–37.7 meV [95]. Note that these values are obtained with the above-discussed, modified Werner models that comprise an exponent similar to the Werner model but with modified prefactors. As these values are mostly lower than $k_BT \approx 25$ meV at room temperature, the criterion $E_B \gg k_BT$ is not fulfilled and the application of the Werner model seems questionable.

The integration of Fermi-Dirac statistics into a model of fluctuating grain-boundary barrier heights is presented by Kajikawa [96]. He evaluates the expression for the conductivity

$$\sigma_{\mathrm{TE}} = \frac{e^2n\langle\tau\rangle}{m^*} = \int_0^\infty\left\{\int_{E_B}^\infty D(E,T)f(E,T)\tau(E,T)dE\right\}P(E_B)dE_B \tag{B9}$$

with $\tau(E,T) = \lambda_g/\nu$ being the relaxation time defined as the fraction of electron mean free path λ_g and electron group velocity ν. The inner integral can be solved and gives the conductivity for uniform barrier heights

$$\sigma_{\mathrm{TE}}^u = \frac{4}{3}\lambda_g\frac{eA^*}{k_B}T\left\{\frac{E_B+E_F}{k_BT}\left[1+\exp\left(\frac{E_B}{k_BT}\right)\right]^{-1} + \ln\left[1+\exp\left(-\frac{E_B}{k_BT}\right)\right]\right\}. \tag{B10}$$

For $E_B \gg k_BT$, Eq. (B10) should reproduce Eq. (B5). However, Eq. (B10) differs from Eq. (B5) by a factor of $8(E_B+E_F)/3k_BT$. Kajikawa's expression gives hence a different temperature dependence than the expression derived by the Schottky barrier theory. The outer integral of Eq. (B9) has to be evaluated numerically. Kajikawa fits temperature-dependent conductivity data of various polycrystalline semiconductors with the three fitting parameters mean free path λ_g, standard deviation, and mean value of the barrier fluctuations. His model includes specifically the condition $E_B \le k_BT$. The price to pay is the lacking analytical solution in the case of fluctuating barriers.

APPENDIX C: FIELD EMISSION—EVALUATION OF COEFFICIENTS

The evaluation of the coefficients b_1, c_1, and f_1 needs the definition of the barrier $\phi(x)$. Using the abrupt depletion approximation, a simple parabolic expression for the Schottky barrier potential

$$\phi(x) = a(x-l)^2 \quad \text{with} \quad a = \frac{e^2n}{2\epsilon_0\epsilon_r}, \quad l = \left[\frac{2\epsilon_0\epsilon_r}{e^2n}(E_B - \mathrm{eV} + E_F)\right]^{1/2} \tag{C1}$$

can be given. n is the carrier concentration, e is the electron charge, and ϵ_0 and ϵ_r are the static dielectric constant and the vacuum permittivity, respectively. l describes the width

of the depletion zone. It is defined by the barrier height E_B, the Fermi level E_F, and the applied voltage V. The abrupt depletion approximation assumes the carrier density to fall abruptly from the density in the bulk to a negligible value in the depletion zone. This simplification might be too drastic in the degenerate case as also pointed out by Padovani and Stratton [98]. However, the excellent agreement between the theory and experiment in the case of metal-semiconductor contacts supports this simplification [50]. Thus, we assume that an appropriate description of the barrier potential is, in fact, obtained under the assumption of the abrupt depletion approximation. Note that, in contrast to us, Garcia-Cuenca, Morenza, and Esteve are indeed able to consider the degeneracy for the barrier potential. Thus, their tunneling model for grain boundaries is more accurate with respect to the actual shape of the barrier than ours.

The coefficient b_1 is defined as

$$b_1 = \alpha \int_{x_1}^{x_2} [\phi(x) - E_F]^{1/2} dx \tag{C2}$$

with $\alpha = 2(2m^*)^{1/2}/\hbar$. The condition $\phi = E_F$ yields x_1 and x_2. Inserting ϕ into Eq. (C2) and performing a hyperbolic substitution gives

$$\begin{aligned} b_1 &= -\frac{\alpha E_F}{\sqrt{a}} \int_{w_1}^{w_2} [\sinh(w)]^2 dw \\ \text{with} \quad w_1 &= 0, \\ w_2 &= \operatorname{arccosh}\left(\sqrt{\frac{a}{E_F}} l\right). \end{aligned} \tag{C3}$$

The antiderivative of this integral is $1/2[\sinh(w)\cosh(w) - w]$. One defines

$$\tilde{E} = \frac{E_B - \mathrm{eV}}{E_F}, \tag{C4}$$

$$E_{00} = \frac{2e}{\alpha} \sqrt{\frac{n}{2\epsilon_0 \epsilon_r}} = \frac{\hbar}{2} \sqrt{\frac{n}{\epsilon_0 \epsilon_r m^*}} \tag{C5}$$

and obtains

$$b_1 = 2 \frac{E_F}{E_{00}} \left[\sqrt{\tilde{E}^2 + \tilde{E}} - \ln\left(\sqrt{\tilde{E} + 1} + \sqrt{\tilde{E}} \right) \right]. \tag{C6}$$

As the integral in Eq. (C2) is axially symmetric with respect to the energy axis, b_1 for a double Schottky barrier is just twice the value of a simple Schottky barrier. Hence, one finds a factor of 2 in Eq. (C6).

The coefficient c_1 is defined as

$$c_1 = \frac{1}{2} \alpha \int_{x_1}^{x_2} [\phi(x) - E_F]^{-1/2} dx. \tag{C7}$$

A hyperbolic substitution results in the expression

$$\begin{aligned} c_1 &= \frac{\alpha}{2\sqrt{a}} \int_{w_1}^{w_2} w dw \\ \text{with} \quad w_1 &= \operatorname{arccosh}\left(\sqrt{\frac{a}{E_F}} l \right), \\ w_2 &= 0. \end{aligned} \tag{C8}$$

The evaluation of the integral leads to

$$c_1 = 2 \frac{1}{E_{00}} \ln\left(\sqrt{\tilde{E} + 1} + \sqrt{\tilde{E}} \right) \tag{C9}$$

with the factor 2 for a double Schottky barrier.

The coefficient f_1 is defined as

$$f_1 = \frac{\alpha}{4} \Bigg[\overbrace{\frac{1}{x_2 - x_1} \left\{ \frac{1}{\phi'(x_1)} - \frac{1}{\phi'(x_2)} \right\} \int_{x_1}^{x_2} [\phi(x) - E_F]^{-1/2} dx}^{\equiv f_{11}} - \underbrace{\frac{1}{2} \int_{x_1}^{x_2} [\phi(x) - E_F]^{-3/2} \left\{ 1 - \frac{\phi'(x)}{x_2 - x_1} \left(\frac{x - x_1}{\phi'(x_2)} + \frac{x_2 - x}{\phi'(x_1)} \right) \right\} dx}_{\equiv f_{12}} \Bigg]. \tag{C10}$$

The upper part f_{11} of Eq. (C10) can be solved easily, as the integral resembles the one of c_1. The result is

$$f_{11} \approx \frac{1}{4E_F \sqrt{a(\tilde{E} + 1)}} \ln(4\tilde{E}). \tag{C11}$$

Note that the approximation

$$\ln\left(\sqrt{\tilde{E} + 1} + \sqrt{\tilde{E}} \right) \approx \ln(4\tilde{E}) \tag{C12}$$

is used. The lower part f_{12} of Eq. (C10) consists of the difference between two diverging integrals. Stratton

circumvents this problem by introducing a special linear transformation [11]. Here, the obstacle is removed by solving the expression

$$f_{12} = \int_{x_1}^{x_2}\{\ldots\} = \lim_{\tilde{x}\to x_2}\int_{x_1}^{\tilde{x}}\{\ldots\} = \frac{\sqrt{\tilde{E}} - \frac{1}{2}\ln(4\tilde{E})}{2E_F\sqrt{a(\tilde{E}+1)}} \tag{C13}$$

with the mathematical software tool *Mathematica* by Wolfram Research. The combination of Eqs. (C11) and (C13) yields

$$f_1 = 2\frac{1}{4E_{00}E_F}\sqrt{\frac{\tilde{E}}{\tilde{E}+1}} = 2\frac{1}{4E_{00}E_F}\sqrt{\frac{E_B - \mathrm{eV}}{E_B - \mathrm{eV} + E_F}}. \tag{C14}$$

Again, the factor of 2 marks the difference between a simple and a double Schottky barrier.

Equation (C14) differs from the expression

$$f_1 = 2\frac{1}{4E_{00}E_F}\sqrt{\frac{E_B}{E_B - E_F}} \tag{C15}$$

given by Padovani [51]. Two reasons favor our result: (i) Let us assume a Schottky barrier with a highly doped semiconductor. In that case, it holds that $k_BT/E_{00} \ll 1$. Thus, field emission should be the dominant transport mechanism. Furthermore, we assume that E_F measured with respect to the conduction band is large and that E_B measured with respect to the Fermi level is small. In particular, $E_B < E_F$ might occur. Using Padovani's expression, this situation would imply that f_1 is not defined. In consequence, the inequality $1 > k_BT(\sqrt{2f_1} + c_1)$ cannot be computed. But that would be a contradiction, as the inequality relation must be fulfilled in the case of field emission. (ii) A situation as described above occurs if one chooses $n = 2\times10^{20}$ cm^{-3} and $Q_t = 7\times10^{13}$ cm^{-2}. It yields $E_F = 459$ meV and $E_B = 206$ meV; thus, $E_B < E_F$. We solve Eq. (C10) numerically for the above-given parameters using the scipy package of Python. We obtain a perfect agreement between the numerical result and Eq. (C14).

For $E_B \gg E_F$ and small applied voltages, Eqs. (C6), (C9), and (C14) can be simplified, respectively, to

$$b_1 = 2\frac{E_B - \mathrm{eV}}{E_{00}}, \tag{C16}$$

$$c_1 = 2\frac{1}{2E_{00}}\ln(4\tilde{E}), \tag{C17}$$

$$f_1 = 2\frac{1}{4E_{00}E_F}. \tag{C18}$$

These expressions, except for the factor of 2, are given by Padovani and Stratton for simple Schottky barriers in their publication [98].

APPENDIX D: THERMIONIC FIELD EMISSION

Thermionic field emission describes the tunneling of electrons at an energy E_m exceeding the Fermi energy E_F but being below the barrier height E_B. E_m is defined by the relation

$$c_m k_B T = 1, \tag{D1}$$

and the J-V characteristic for thermionic field emission is described by [51,98,99]

$$J_{\mathrm{TFE}} = \frac{A^*T}{2\pi k_B}\exp\left(\frac{E_F}{k_BT} - b_m - \frac{E_m}{k_BT}\right)\left(\frac{\pi}{f_m}\right)^{1/2} \times\left[1 - \exp\left(-\frac{\mathrm{eV}}{k_BT}\right)\right]. \tag{D2}$$

b_m, c_m, and f_m are the tunneling coefficients derived in Appendix C. The expressions for the thermionic field emission coefficients b_m, c_m, and f_m differ from those of pure field emission b_1, c_1, and f_1 only by the replacement of the Fermi level E_F by the characteristic energy E_m. Note that this not only implies the modification of the integrand, but also of the integration limits now defined by $\phi(x) = E_m$. Evaluating the coefficients according to Appendix C results in

$$b_m = 2\frac{1}{E_{00}}\left[\sqrt{\bar{E} - E_m}\sqrt{\bar{E}} - \frac{E_{00}E_m}{2k_BT}\right], \tag{D3}$$

$$c_m = 2\frac{1}{E_{00}}\ln\left\{\frac{\sqrt{\bar{E} - E_m}\sqrt{\bar{E}}}{\sqrt{E_m}}\right\}, \tag{D4}$$

$$f_m = 2\frac{1}{4E_{00}E_m}\sqrt{\frac{\tilde{E}^m}{\tilde{E}^m + 1}} \tag{D5}$$

$$\approx 2\frac{\cosh^2(E_{00}/2k_BT)}{4E_{00}\bar{E}}\frac{1}{\sqrt{2 - \tanh^2(E_{00}/2k_BT)}} \tag{D6}$$

with the parameters

$$\bar{E} = E_B + E_F - \mathrm{eV}, \tag{D7}$$

$$\tilde{E}^m = \frac{E_B - \mathrm{eV}}{E_m}, \tag{D8}$$

$$E_m = \frac{\bar{E}}{\cosh^2(E_{00}/2k_BT)}. \tag{D9}$$

The expression for E_m is deduced by inserting c_m into Eq. (D1). Equation (D1) is also used to derive the term $E_{00}E_m/k_BT$ in the expression for b_m. Equation (D6) is obtained from Eq. (D5) by applying the expression for E_m and by evaluating the square-root term in (D5). The examination of the exponent in Eq. (D2) reveals that

$$b_m - \frac{E_m}{k_BT} = 2\frac{\bar{E}}{E_0}, \tag{D10}$$

$$\text{where } E_0 = E_{00}\coth\left(\frac{E_{00}}{2k_BT}\right). \tag{D11}$$

The thermionic field emission current J_{TFE} can thus be expressed as

$$\begin{aligned} J_{\mathrm{TFE}} = {} & \frac{A^*T\sqrt{E_{00}\bar{E}}}{\sqrt{2\pi}k_B\cosh\left(E_{00}/2k_BT\right)}\left[2-\tanh^2(E_{00}/2k_BT)\right]^{1/4} \\ & \times\exp\left\{\frac{E_F}{k_BT}-2\frac{E_B+E_F}{E_0}\right\}\exp\left(2\frac{\mathrm{eV}}{E_0}\right) \\ & \times\left[1-\exp\left\{-\frac{\mathrm{eV}}{k_BT}\right\}\right]. \end{aligned} \tag{D12}$$

Using Eq. (17), one obtains the conductivity

$$\begin{aligned} \sigma_{\mathrm{TFE}} = {} & \frac{eLA^*\sqrt{E_{00}(E_B+E_F)}}{\sqrt{2\pi}k_B^2\cosh\left(E_{00}/2k_BT\right)}\left[2-\tanh^2(E_{00}/2k_BT)\right]^{1/4} \\ & \times\exp\left(\frac{E_F}{k_BT}\right)\exp\left\{-2\frac{E_B+E_F}{E_0}\right\}. \end{aligned} \tag{D13}$$

Expression (D13) differs from the one derived by Yu [52]. Instead of the term $[2-\tanh^2(E_{00}/k_BT)]^{1/4}$, Yu's equation contains the expression $\sqrt{\coth(E_{00}/k_BT)}$. This difference is a direct consequence of the discrepancy between Padovani's expression for f_1 and the one derived in this work (see Appendix C).

Fluctuating barriers can be implemented into the model of thermionic field emission according to the procedure proposed by Werner. The procedure is outlined in Appendix B. As a result, Eq. (D13) is modified by an additional factor. The conductivity σ^f_{TFE} comprising fluctuating barriers is thus given by

$$\sigma^f_{\mathrm{TFE}} = \sigma_{\mathrm{TFE}}\times\exp\left(\frac{\tilde{\sigma}_B^2}{2E_{00}}\right). \tag{D14}$$

Similar to the thermionic emission case, fluctuating barriers induce a reduction of the barrier height. The reduction is given by $\tilde{\sigma}_B^2/2E_{00}$.

APPENDIX E: FIELD EMISSION AND FLUCTUATING BARRIERS

Fluctuating barriers are implemented into the tunneling equations according to the approach by Werner for thermionic emission outlined in Appendix B [93]. The current density J_{FE} is multiplied with a Gaussian distribution $P(E_B)$ resembling the barrier fluctuations. This expression is then integrated over the barrier energy E_B. One obtains the expression for the conductivity

$$\begin{aligned} \sigma^f_{\mathrm{FE}}(\bar{E}_B,\tilde{\sigma}_B) &= L\frac{d}{dV}\int_{-\infty}^{\infty}J_{\mathrm{FE}}(E_B)P(E_B)DE_B \\ &= L\int_{-\infty}^{\infty}\frac{dJ(E_B)}{dV}P(E_B)DE_B \\ &= \int_{-\infty}^{\infty}\sigma_{\mathrm{FE}}(E_B)P(E_B)dE_B \end{aligned} \tag{E1}$$

by interchanging derivation and integration. $\sigma_{\mathrm{FE}}(E_B)$ is described by Eq. (18). It is repeated here for completeness:

$$\sigma_{\mathrm{FE}} = \frac{eLA^*c_1}{(c_1k_B)^2}\exp\left(-b_1\right)\left\{\frac{\pi c_1k_BT}{\sin\left(\pi c_1k_BT\right)}-\exp\left(-c_1E_F\right)\right\}. \tag{E2}$$

The exponential functions as well as their prefactors contain the integration variable E_B. However, the exponential functions are considered for the integration only. In the prefactors, one defines $E_B = \bar{E}_B$. The integrals to solve are thus

$$\int_{-\infty}^{\infty}\exp(\underbrace{-b_1}_{\equiv e_1})P(E_B)dE_B \tag{E3}$$

$$\text{and}\quad \int_{-\infty}^{\infty}\exp(\underbrace{-b_1-c_1E_F}_{\equiv e_2})P(E_B)dE_B. \tag{E4}$$

The expressions e_1 and e_2 have to be simplified in order to perform the integration, because these expressions contain the parameters b_1 and c_1, which are rather complex functions of the integration variable E_B. Fits using the uniform barrier height model yield values $\tilde{E}<1$. Therefore, $\tilde{E}\ll 1$ is assumed for the approximation of e_1 and e_2.

First, the expression

$$e_1 = -b_1 = -2\frac{E_F}{E_{00}}\left[\underbrace{\sqrt{\tilde{E}^2+\tilde{E}}}_{\approx\sqrt{\tilde{E}}}-\underbrace{\ln\left(\sqrt{\tilde{E}+1}+\sqrt{\tilde{E}}\right)}_{\equiv(\star)}\right] \tag{E5}$$

is estimated. The term $(\star)$ can be further simplified:

$$
\begin{aligned}
(\star) &= \ln\left\{\sqrt{\tilde{E}+1}+\sqrt{\tilde{E}}\right\} \\
&= \ln\left\{\sqrt{\left(\sqrt{\tilde{E}+1}+\sqrt{\tilde{E}}\right)^2}\right\} \\
&= \ln\left\{\sqrt{\tilde{E}+1+2\sqrt{\tilde{E}^2+\tilde{E}}+\tilde{E}}\right\} \\
&\approx \ln\left\{\sqrt{2\sqrt{\tilde{E}}+1}\right\} \\
&= \frac{1}{2}\ln\left\{2\sqrt{\tilde{E}}+1\right\} \\
&\approx \frac{1}{2}\left(2\sqrt{\tilde{E}}-\frac{4\tilde{E}}{2}\right) \\
&= \sqrt{\tilde{E}}-\tilde{E} \qquad \text{(E6)}
\end{aligned}
$$

by taking the square and the square root in the argument of the logarithm and using the relation $\ln(x^{1/2}) = 1/2\ln(x)$. Furthermore, one can expand the logarithm into a power series according to the expression $\ln(x+1) \approx x - x^2/2$. The power series converges for $|x| < 1$. Accordingly, the boundary condition for Eq. (E6) is $\tilde{E} < 1/4$. Inserting Eq. (E6) into Eq. (E5), one obtains

$$
\begin{aligned}
e_1 = -b_1 &= -2\frac{E_F}{E_{00}}\left[\sqrt{\tilde{E}}-\sqrt{\tilde{E}}+\tilde{E}\right] \\
&= -2\frac{E_F}{E_{00}}\tilde{E} = -2\frac{E_B}{E_{00}}. \qquad \text{(E7)}
\end{aligned}
$$

The relation $\tilde{E} = E_B/E_F$ is used for the last transformation. Finally, a numerical comparison of the full and approximated expression for e_1 reveals that the best agreement is achieved by

$$
e_1 = -b_1 = -\frac{E_B}{2E_{00}}. \qquad \text{(E8)}
$$

Next, the expression e_2 has to be evaluated for $\tilde{E} \ll 1$. The approximation is

$$
\begin{aligned}
e_2 &= -b_1 - c_1 E_F \\
&= -2\frac{E_F}{E_{00}}\sqrt{\tilde{E}^2+\tilde{E}} \\
&\approx -2\frac{E_F}{E_{00}}\sqrt{\tilde{E}} \\
&= -2\frac{E_F}{E_{00}}\sqrt{\frac{E_B}{E_F}}. \qquad \text{(E9)}
\end{aligned}
$$

Inserting Eqs. (E8) and (E9) into expressions (E3) and (E4) yields

$$
\int_{-\infty}^{\infty} \exp\left(-\frac{E_B}{2E_{00}}\right) P(E_B)\,dE_B \qquad \text{(E10)}
$$

and

$$
\int_{-\infty}^{\infty} \exp\left(-2\frac{E_F}{E_{00}}\sqrt{\frac{E_B}{E_F}}\right) P(E_B)\,dE_B. \qquad \text{(E11)}
$$

The integrand (E11) is not defined for $E_B < 0$. Therefore, the integral (E11) cannot be solved. In contrast, integral (E10) is solvable. One obtains the expression

$$
\begin{aligned}
&\int_{-\infty}^{\infty} \exp\left(-\frac{E_B}{2E_{00}}\right) P(E_B)\,dE_B \\
&\quad = \exp\left\{-\frac{1}{2E_{00}}\left(\bar{E}_B - \frac{\tilde{\sigma}_B^2}{4E_{00}}\right)\right\} \qquad \text{(E12)}
\end{aligned}
$$

with $\tilde{\sigma}_B$ being the standard deviation around the mean value $\bar{E}_B$.

The comparison of the first and second summands of Eq. (E2) reveals the first summand to be roughly one order of magnitude larger than the second one. Potential fluctuations might thus be neglected in the second term. This assumption is beneficial, because the second summand contains the integral that is analytically unsolvable. The final equation describing tunneling through fluctuating barriers is thus given by

$$
\begin{aligned}
\sigma_{\mathrm{FE}}^{f} = &\frac{eLA^*\pi T}{k_B \sin(\pi \bar{c}_1 k_B T)} \exp\left\{-\frac{1}{2E_{00}}\left(\bar{E}_B - \frac{\tilde{\sigma}_B^2}{4E_{00}}\right)\right\} \\
&- \frac{eLA^*\bar{c}_1}{(\bar{c}_1 k_B)^2} \exp\left\{-\bar{b}_1 - \bar{c}_1 E_F\right\} \qquad \text{(E13)}
\end{aligned}
$$

in which the parameters

$$
\bar{b}_1 = b_1(\bar{E}_B) \quad \text{and} \quad \bar{c}_1 = c_1(\bar{E}_B) \qquad \text{(E14)}
$$

are defined.

[1] K. L. Chopra, P. D. Paulson, and V. Dutta, Thin-film solar cells: An overview, Prog. Photovoltaics **12**, 69 (2004).

[2] K. Ellmer, A. Klein, and B. Rech, *Transparent Conductive Zinc Oxide: Basics and Applications in Thin Film Solar Cells* (Springer, New York, 2007), Vol. 104.

[3] A. G. Aberle, Thin-film solar cells, Thin Solid Films **517**, 4706 (2009).

[4] C. G. Granqvist, Transparent conductors as solar energy materials: A panoramic review, Sol. Energy Mater. Sol. Cells **91**, 1529 (2007).

[5] C. G. Granqvist, *Handbook of Inorganic Electrochromic Materials* (Elsevier, New York, 1995).

[6] D. S. Ginley and C. Bright, Transparent conducting oxides, MRS Bull. **25**, 15 (2000).

[7] J. Y. W. Seto, The electrical properties of polycrystalline silicon films, J. Appl. Phys. **46**, 5247 (1975).

[8] R. L. Petritz, Theory of photoconductivity in semiconductor films, Phys. Rev. **104**, 1508 (1956).

[9] S. Sze and K. Ng, *Physics of Semiconductor Devices* (Wiley, New York, 2006).

[10] J. Orton, Interpretation of Hall mobility in polycrystalline thin films, Thin Solid Films **86**, 351 (1981).

[11] R. Stratton, Volt-current characteristics for tunneling through insulating films, J. Phys. Chem. Solids **23**, 1177 (1962).

[12] R. Stratton, Theory of field emission from semiconductors, Phys. Rev. **125**, 67 (1962).

[13] Y. S. Jung, O. V. Kononenko, and W.-K. Choi, Electron transport in high quality undoped ZnO film grown by plasma-assisted molecular beam epitaxy, Solid State Commun. **137**, 474 (2006).

[14] K. Ellmer and R. Mientus, Carrier transport in polycrystalline transparent conductive oxides: A comparative study of zinc oxide and indium oxide, Thin Solid Films **516**, 4620 (2008).

[15] D. Gerthsen, D. Litvinov, T. Gruber, C. Kirchner, and A. Waag, Origin and consequences of a high stacking fault density in epitaxial ZnO layers, Appl. Phys. Lett. **81**, 3972 (2002).

[16] D. S. Ginley *et al.*, *Handbook of Transparent Conductors* (Springer, New York, 2011).

[17] D. Mergel and Z. Qiao, Correlation of lattice distortion with optical and electrical properties of In_2O_3 : Sn films, J. Appl. Phys. **95**, 5608 (2004).

[18] B. D. Ahn, S. H. Oh, H. J. Kim, M. H. Jung, and Y. G. Ko, Low temperature conduction and scattering behavior of Ga-doped ZnO, Appl. Phys. Lett. **91**, 252109 (2007).

[19] V. Bhosle, A. Tiwari, and J. Narayan, Electrical properties of transparent and conducting Ga doped ZnO, J. Appl. Phys. **100**, 033713 (2006).

[20] Z. Ovadyahu, Nonequilibrium dephasing in two-dimensional indium oxide films, Phys. Rev. B **63**, 235403 (2001).

[21] K. Ellmer, Resistivity of polycrystalline zinc oxide films: Current status and physical limit, J. Phys. D **34**, 3097 (2001).

[22] E. Conwell and V. F. Weisskopf, Theory of impurity scattering in semiconductors, Phys. Rev. **77**, 388 (1950).

[23] H. Brooks, *Advances in Electronics and Electron Physics* (Academic, New York, 1955).

[24] R. Dingle, XCIV. Scattering of electrons and holes by charged donors and acceptors in semiconductors, Philos. Mag. **46**, 831 (1955).

[25] Brooks and Herring derived an expression for nondegenerate semiconductors. Dingle adapted it for degenerate semiconductors.

[26] T. Pisarkiewicz, K. Zakrzewska, and E. Leja, Scattering of charge carriers in transparent and conducting thin oxide films with a non-parabolic conduction band, Thin Solid Films **174**, 217 (1989).

[27] Note that the expression for ξ_0 has a minor fault in Ref. [26] as, for example, mentioned by Kajikawa [28].

[28] Y. Kajikawa, Effects of grain-boundary potential barrier height and its fluctuation on conductivity of polycrystalline semiconductors in the ionized-impurity-scattering dominated case, J. Appl. Phys. **114**, 043719 (2013).

[29] J. Ziman, *Electrons and Phonons: The Theory of Transport Phenomena in Solids, Oxford Classic Texts in the Physical Sciences* (Oxford University, New York, 2001).

[30] P. B. Allen, in *Quantum Theory of Real Metals*, edited by J. R. C. S. G. Louie (Kluwer Academic, Dordrecht, 1996), Chap. 17, pp. 219–250.

[31] S. Hunklinger, *Festkörperphysik* (Oldenbourg Verlag, 2007).

[32] D. C. Look, K. D. Leedy, L. Vines, B. G. Svensson, A. Zubiaga, F. Tuomisto, D. R. Doutt, and L. J. Brillson, Self-compensation in semiconductors: The Zn vacancy in Ga-doped ZnO, Phys. Rev. B **84**, 115202 (2011).

[33] X. D. Liu, J. Liu, S. Chen, and Z. Q. Li, Electrical transport properties of Al-doped ZnO films, Appl. Surf. Sci. **263**, 486 (2012).

[34] D. Zhang and H. Ma, Scattering mechanisms of charge carriers in transparent conducting oxide films, Appl. Phys. A **62**, 487 (1996).

[35] B.-T. Lin, Y.-F. Chen, J.-J. Lin, and C.-Y. Wu, Temperature dependence of resistance and thermopower of thin indium tin oxide films, Thin Solid Films **518**, 6997 (2010).

[36] H. Y. Liu, V. Avrutin, N. Izyumskaya, Ü. Özgür, A. B. Yankovich, A. V. Kvit, P. M. Voyles, and H. Morkoç, Electron scattering mechanisms in GZO films grown on a-sapphire substrates by plasma-enhanced molecular beam epitaxy, J. Appl. Phys. **111**, 103713 (2012).

[37] T. Terasako, H. Song, H. Makino, S. Shirakata, and T. Yamamoto, Temperature dependence of electrical properties of Ga-doped ZnO films deposited by ion plating with DC arc discharge, Thin Solid Films **528**, 19 (2013).

[38] A. Bikowski and K. Ellmer, Analytical model of electron transport in polycrystalline, degenerately doped ZnO films, J. Appl. Phys. **116**, 143704 (2014).

[39] Note that field emission is also denoted as tunneling.

[40] A. P. Roth and D. F. Williams, Properties of zinc oxide films prepared by the oxidation of diethyl zinc, J. Appl. Phys. **52**, 6685 (1981).

[41] A. Kronenberger, A. Polity, D. M. Hofmann, B. K. Meyer, A. Schleife, and F. Bechstedt, Structural, electrical, and optical properties of hydrogen-doped ZnO films, Phys. Rev. B **86**, 115334 (2012).

[42] S. Brehme, F. Fenske, W. Fuhs, E. Nebauer, M. Poschenrieder, B. Selle, and I. Sieber, Free-carrier plasma resonance effects and electron transport in reactively sputtered degenerate ZnO : Al films, Thin Solid Films **342**, 167 (1999).

[43] M. V. Garcia-Cuenca, J. L. Morenza, and J. Esteve, Electron tunneling in heavily In-doped polycrystalline CdS films, J. Appl. Phys. **56**, 1738 (1984).

[44] M. Ada-Hanifi, J. Sicart, J. M. Dusseau, and J. L. Robert, A model of conduction in polycrystalline silicon films, J. Appl. Phys. **62**, 1869 (1987).

[45] R. Holm, The electric tunnel effect across thin insulator films in contacts, J. Appl. Phys. **22**, 569 (1951).

[46] J. G. Simmons, Generalized formula for the electric tunnel effect between similar electrodes separated by a thin insulating film, J. Appl. Phys. **34**, 1793 (1963).

[47] J. G. Simmons, Conduction in thin dielectric films, J. Phys. D **4**, 613 (1971).

[48] H. Kramers, Wellenmechanik und halbzahlige Quantisierung, Z. Phys. **39**, 828 (1926).

[49] G. Wentzel, Eine Verallgemeinerung der Quantenbedingungen für die Zwecke der Wellenmechanik, Z. Phys. **38**, 518 (1926).

[50] E. Rhoderick and R. Williams, *Metal-Semiconductor Contacts, Monographs in Electrical and Electronic Engineering* (Clarendon, Oxford, 1988).

[51] F. Padovani, in *Applications and Devices*, Semiconductors and Semimetals, Vol. 7, Part A, edited by R. Willardson and A. C. Beer (Elsevier, New York, 1971), Chap. 2, pp. 75–146.

[52] A. Yu, Electron tunneling and contact resistance of metal-silicon contact barriers, Solid State Electron. **13**, 239 (1970).

[53] C. Crowell and V. Rideout, Normalized thermionic-field (T-F) emission in metal-semiconductor (Schottky) barriers, Solid State Electron. **12**, 89 (1969).

[54] M. Berginski, Ph.D. thesis, RWTH Aachen University, 2008.

[55] J. Hüpkes, Ph.D. thesis, RWTH Aachen University, 2005.

[56] M. Berginski, J. Hüpkes, M. Schulte, G. Schöpe, H. Stiebig, B. Rech, and M. Wuttig, The effect of front ZnO:Al surface texture and optical transparency on efficient light trapping in silicon thin-film solar cells, J. Appl. Phys. **101**, 074903 (2007).

[57] N. Sommer, M. Stanley, F. Köhler, J. Mock, and J. Hüpkes, Role of the dopant aluminum for the growth of sputtered ZnO:Al investigated by means of a seed layer concept, J. Appl. Phys. **118**, 035301 (2015).

[58] A. Bikowski and K. Ellmer, A comparative study of electronic and structural properties of polycrystalline and epitaxial magnetron-sputtered ZnO:Al and $Zn_{1-x}Mg_xO$:Al Films—Origin of the grain barrier traps, J. Appl. Phys. **114**, 063709 (2013).

[59] T. Minami, H. Sato, K. Ohashi, T. Tomofuji, and S. Takata, Conduction mechanism of highly conductive and transparent zinc oxide thin films prepared by magnetron sputtering, J. Cryst. Growth **117**, 370 (1992).

[60] K. Ellmer and R. Mientus, Carrier transport in polycrystalline ITO and ZnO:Al II: The influence of grain barriers and boundaries, Thin Solid Films **516**, 5829 (2008).

[61] S. Y. Myong, J. Steinhauser, R. Schlüchter, S. Faÿ, E. Vallat-Sauvain, A. Shah, C. Ballif, and A. Rüfenacht, Temperature dependence of the conductivity in large-grained boron-doped ZnO films, Sol. Energy Mater. Sol. Cells **91**, 1269 (2007).

[62] J. I. Kim, W. Lee, T. Hwang, J. Kim, S.-Y. Lee, S. Kang, H. Choi, S. Hong, H. H. Park, T. Moon, and B. Park, Quantitative analyses of damp-heat-induced degradation in transparent conducting oxides, Sol. Energy Mater. Sol. Cells **122**, 282 (2014).

[63] T. Tohsophon, J. Hüpkes, S. Calnan, W. Reetz, B. Rech, W. Beyer, and N. Sirikulrat, Damp heat stability and annealing behavior of aluminum doped zinc oxide films prepared by magnetron sputtering, Thin Solid Films **511–512**, 673 (2006).

[64] J. Steinhauser, S. Faÿ, N. Oliveira, E. Vallat-Sauvain, D. Zimin, U. Kroll, and C. Ballif, Electrical transport in boron-doped polycrystalline zinc oxide thin films, Phys. Status Solidi (a) **205**, 1983 (2008).

[65] S. Faÿ, J. Steinhauser, S. Nicolay, and C. Ballif, Polycrystalline ZnO:B grown by LPCVD as TCO for thin film silicon solar cells, Thin Solid Films **518**, 2961 (2010).

[66] J. Hüpkes, J. Owen, M. Wimmer, F. Ruske, D. Greiner, R. Klenk, U. Zastrow, and J. Hotovy, Damp heat stable doped zinc oxide films, Thin Solid Films **555**, 48 (2014).

[67] J. W. Orton and M. J. Powell, The Hall effect in polycrystalline and powdered semiconductors, Rep. Prog. Phys. **43**, 1263 (1980).

[68] D. Greiner, N. Papathanasiou, A. Pflug, F. Ruske, and R. Klenk, Influence of damp heat on the optical and electrical properties of Al-doped zinc oxide, Thin Solid Films **517**, 2291 (2009).

[69] D. Greiner, S. Gledhill, C. Köble, J. Krammer, and R. Klenk, Damp heat stability of Al-doped zinc oxide films on smooth and rough substrates, Thin Solid Films **520**, 1285 (2011).

[70] The meaning of "deep" relates to the energetic state below the Fermi level for all doping levels.

[71] A. Bikowski, M. Rengachari, M. Nie, N. Wanderka, P. Stender, G. Schmitz, and K. Ellmer, Inhomogeneous aluminium dopant distribution in magnetron sputtered ZnO:Al thin films and its influence on their electrical properties, APL Mater. **3**, 060701 (2015).

[72] E. M. Likovich, R. Jaramillo, K. J. Russell, S. Ramanathan, and V. Narayanamurti, Scanning tunneling microscope investigation of local density of states in Al-doped ZnO thin films, Phys. Rev. B **83**, 075430 (2011).

[73] S. C. Abrahams and J. L. Bernstein, Remeasurement of the structure of hexagonal ZnO, Acta Crystallogr. Sect. B **25**, 1233 (1969).

[74] U. Özgür, Y. I. Alivov, C. Liu, A. Teke, M. A. Reshchikov, S. Doan, V. Avrutin, S.-J. Cho, and H. Morko, A comprehensive review of ZnO materials and devices, J. Appl. Phys. **98**, 041301 (2005).

[75] R. R. Reeber, Lattice parameters of ZnO from 4.2 to 296 K, J. Appl. Phys. **41**, 5063 (1970).

[76] A. Hutson, Electronic properties of ZnO, J. Phys. Chem. Solids **8**, 467 (1959).

[77] X. X. Yang, Z. F. Zhou, Y. Wang, R. Jiang, W. T. Zheng, and C. Q. Sun, Raman spectroscopy determination of the Debye temperature and atomic cohesive energy of CdS, CdSe, Bi_2Se_3, and Sb_2Te_3 nanostructures, J. Appl. Phys. **112**, 083508 (2012).

[78] Y. Sato, Investigation of microstructure and its impact on physical property in electroceramics, J. Ceram. Soc. Jpn. **121**, 825 (2013).

[79] W. Körner and C. Elssser, First-principles density functional study of dopant elements at grain boundaries in ZnO, Phys. Rev. B **81**, 085324 (2010).

[80] A. Janotti and C. G. Van de Walle, Native point defects in ZnO, Phys. Rev. B **76**, 165202 (2007).

[81] F. Ruske, A. Pflug, V. Sittinger, B. Szyszka, D. Greiner, and B. Rech, Optical modeling of free electron behavior in highly doped ZnO films, Thin Solid Films **518**, 1289 (2009).

[82] H. Fujiwara and M. Kondo, Effects of carrier concentration on the dielectric function of ZnO:Ga and In_2O_3:Sn studied by spectroscopic ellipsometry: Analysis of free-carrier and band-edge absorption, Phys. Rev. B **71**, 075109 (2005).

[83] D. L. Young, T. J. Coutts, V. I. Kaydanov, A. S. Gilmore, and W. P. Mulligan, Direct measurement of density-of-states

effective mass and scattering parameter in transparent conducting oxides using second-order transport phenomena, J. Vac. Sci. Technol. A **18**, 2978 (2000).

[84] S. Cornelius, M. Vinnichenko, N. Shevchenko, A. Rogozin, A. Kolitsch, and W. Möller, Achieving high free electron mobility in ZnO:Al thin films grown by reactive pulsed magnetron sputtering, Appl. Phys. Lett. **94**, 042103 (2009).

[85] N. Sommer, Ph.D. thesis, RWTH Aachen University, 2016.

[86] M. Warzecha, J. I. Owen, M. Wimmer, F. Ruske, J. Hotovy, and J. Hüpkes, High mobility annealing of transparent conductive oxides, IOP Conf. Ser.: Mater. Sci. Eng. **34**, 012004 (2012).

[87] D. C. Look, T. C. Droubay, and S. A. Chambers, Stable highly conductive ZnO via reduction of Zn vacancies, Appl. Phys. Lett. **101**, 102101 (2012).

[88] Z.-C. Jin, I. Hamberg, and C. G. Granqvist, Optical properties of sputter-deposited ZnO:Al thin films, J. Appl. Phys. **64**, 5117 (1988).

[89] J. Steinhauser, S. Fay, N. Oliveira, E. Vallat-Sauvain, and C. Ballif, Transition between grain boundary and intragrain scattering transport mechanisms in boron-doped zinc oxide thin films, Appl. Phys. Lett. **90**, 142107 (2007).

[90] Z. Qiao, C. Agashe, and D. Mergel, Dielectric modeling of transmittance spectra of thin ZnO:Al films, Thin Solid Films **496**, 520 (2006).

[91] C. Crowell and S. Sze, Current transport in metal-semiconductor barriers, Solid State Electron. **9**, 1035 (1966).

[92] A voltage of 1 V is applied during Hall measurements across a sample size of approximately 1 cm. Assuming a grain size of 40 nm, the voltage of 1 V is distributed across 1 cm/40 nm = 250 000 grain boundaries. The voltage drop at each of these 250 000 grain boundaries is thus roughly 1 μV. Consequently, it holds at room temperature that 1×10^{-6} eV $\ll 25 \times 10^{-3}$ eV $= k_B T$.

[93] J. H. Werner and H. H. Güttler, Barrier inhomogeneities at Schottky contacts, J. Appl. Phys. **69**, 1522 (1991).

[94] J. Werner, Origin of curved Arrhenius plots for the conductivity of polycrystalline semiconductors, Solid State Phenom. **37**, 213 (1994).

[95] J. Oertel, K. Ellmer, W. Bohne, J. Röhrich, and H. Tributsch, Growth of n-type polycrystalline pyrite (FeS_2) films by metalorganic chemical vapour deposition and their electrical characterization, J. Cryst. Growth **198–199**, 1205 (1999).

[96] Y. Kajikawa, Conduction model covering non-degenerate through degenerate polycrystalline semiconductors with non-uniform grain-boundary potential heights based on an energy filtering model, J. Appl. Phys. **112**, 123713 (2012).

[97] J. Bruneaux, H. Cachet, M. Froment, and A. Messad, Correlation between structural and electrical properties of sprayed tin oxide films with and without fluorine doping, Thin Solid Films **197**, 129 (1991).

[98] F. Padovani and R. Stratton, Field and thermionic-field emission in Schottky barriers, Solid State Electron. **9**, 695 (1966).

[99] R. Stratton, Diffusion of hot and cold electrons in semiconductor barriers, Phys. Rev. **126**, 2002 (1962).